

6 Xenon Detector System

6.1 Overview

The direct observation of WIMP dark matter scattering within a detector of any kind is a significant experimental challenge. Searches for these elusive particles require an extremely sensitive, low-background detector able to separate NR events at the few-keV energy from a dominant background of ER interactions, some created by particles external to the WIMP target and others arising within it from radioactive contaminants. The LZ experiment addresses part of the background issue by operating deep underground, and surrounding the instrument with a set of concentric water and Gd-LS veto shields that are described in detail in Chapter 7. However, observing these small energy depositions in space and time requires a highly instrumented LXe TPC assembled from high-performance, low-radio-background components operating in the cold liquid that have been developed explicitly for this purpose. The design of these elements has been influenced extensively by our collaboration's experience with operating both the LUX and ZEPLIN experiments as described in Chapter 5.

While LXe is inherently a very radio-quiet detector material with enough density and Z to very effectively self-shield from external backgrounds, the design of this new detector nevertheless requires that attention be paid to the radiopurity of a number of significant detector elements, such as the PMTs, support structures, and reflecting surfaces. This imposes serious constraints on material composition and their location, adding significant complication to the instrument's design. The details of these developments will be described in the related sections below.

The Xe detector system includes the TPC and ancillary systems required for its readout, control, and monitoring (cables and conduits, monitoring sensors, etc.). An additional anticoincidence detector is formed by a layer of LXe enveloping the TPC, which we term the "skin" detector. The main components of these two instruments are described in this chapter: the TPC, including HV delivery, PMT systems, and internal liquid flow and monitoring instrumentation; and the skin detector and its readout.

The TPC itself has a three-electrode configuration: a cathode grid at the bottom, a gate grid just below the liquid surface, and an anode grid just above the liquid surface. It features two arrays of PMTs, one immersed in the LXe viewing up, and the other in the gas phase viewing down. The WIMP target contains some 7 tonnes of active LXe, located vertically between the cathode and gate grids and enclosed laterally by a cylindrical arrangement of PTFE reflector panels. Interactions in this region generate prompt VUV scintillation light detected by the PMTs (S1 pulse). The applied electric field sweeps the ionization charge liberated at the interaction site and drifts it upward past the gate electrode; these electrons are extracted into the vapor phase, where they generate electroluminescence — which is again detected by the same two PMT arrays (S2 pulse). This double-phase (liquid/gas) technique, which generates two pulses per interaction, resolves the energy deposition sites with great spatial accuracy down to very low energies, allowing identification of multiple scatter events and, as described previously, providing discrimination between ER and NR interactions.

Table 6.1.1 lists the key design parameters of the Xe detector system and performance specifications needed to meet the scientific goals described previously.

An important enhancement beyond LUX is the treatment of the skin layer of LXe located between the stack of PTFE reflector panels that surround the active region and the cryostat wall, as well as the region beneath the bottom PMT array. A very-high-quality dielectric standoff is needed between the very-high electric field portions of the field cage and the grounded metallic vessel wall. A few-cm-thick layer of LXe is excellent for this role, with the added advantage of allowing measurement of any energy deposited in this layer, from which we read out the scintillation light. Operated as a stand-alone veto, this layer is insufficiently thick to have high efficiency. However, the combination of this skin detector and the outer LS detector forms a highly efficient tag of internal and external backgrounds. The efficiency is further

Table 6.1.1. Major parameters of the Xe detector system.

Item	Parameter
Liquid Xenon	Total mass = 9.6 tonnes Active mass= 7.0 tonnes
Vertical dimensions	
Drift region (cathode-anode)	1.46 m
Extraction region (gate-anode)	1.0 cm (0.5 cm liquid, 0.5 cm gas)
Reverse field region (sub-cathode)	14.0 cm
Lateral dimensions	
TPC Diameter	1.46 m
Field cage wall thickness	2.0 cm
Skin thickness — wall region	Min (max) = 4.0 (8.0) cm
Grid transparencies at normal incidence	
Bottom shield	96 %
Cathode	92 %
Gate	98 %
Anode	76 %
Top shield	99 %
Operating conditions	
Cathode voltage	−100 kV
Gate voltage	−4 kV
Anode voltage	+4 kV
Gas region field	10.6 kV/cm
Drift region field	0.7 kV/cm
Design target highest surface field (in LXe)	50.0 kV/cm
Operating pressure	1.6 bar
Photomultipliers	
TPC 3" Ø phototube count	Top (Bottom) = 247 (241) tubes
Xenon skin 1"-square phototube count	Sides (Bottom) = 120 (60)

enhanced by the overall minimization of inert materials that can absorb gammas and neutrons: The TPC is constructed of the minimum needed mass of PTFE and field-shaping rings, and the vessels and PMT support structures are made of Ti. Both PTFE and Ti are low density and low Z, and thus highly transparent to gamma rays. Important design drivers for the skin are its optical decoupling from the TPC, and compatibility between the skin readout and the TPC HV design.

Another area of major difference between the device proposed here and the previous LUX and ZEPLIN detectors is the side-entry method of bringing in the very-high-voltage connection to the cathode, and the short “reverse-field” region between the cathode and the lower PMT array. This reverse-field region is especially challenging in LZ because of the very-high electric field there, which results from having the highest possible voltage on the cathode while simultaneously minimizing the mass of LXe between the cathode and the bottom PMT array. Our approach to these issues is described below in separate sections

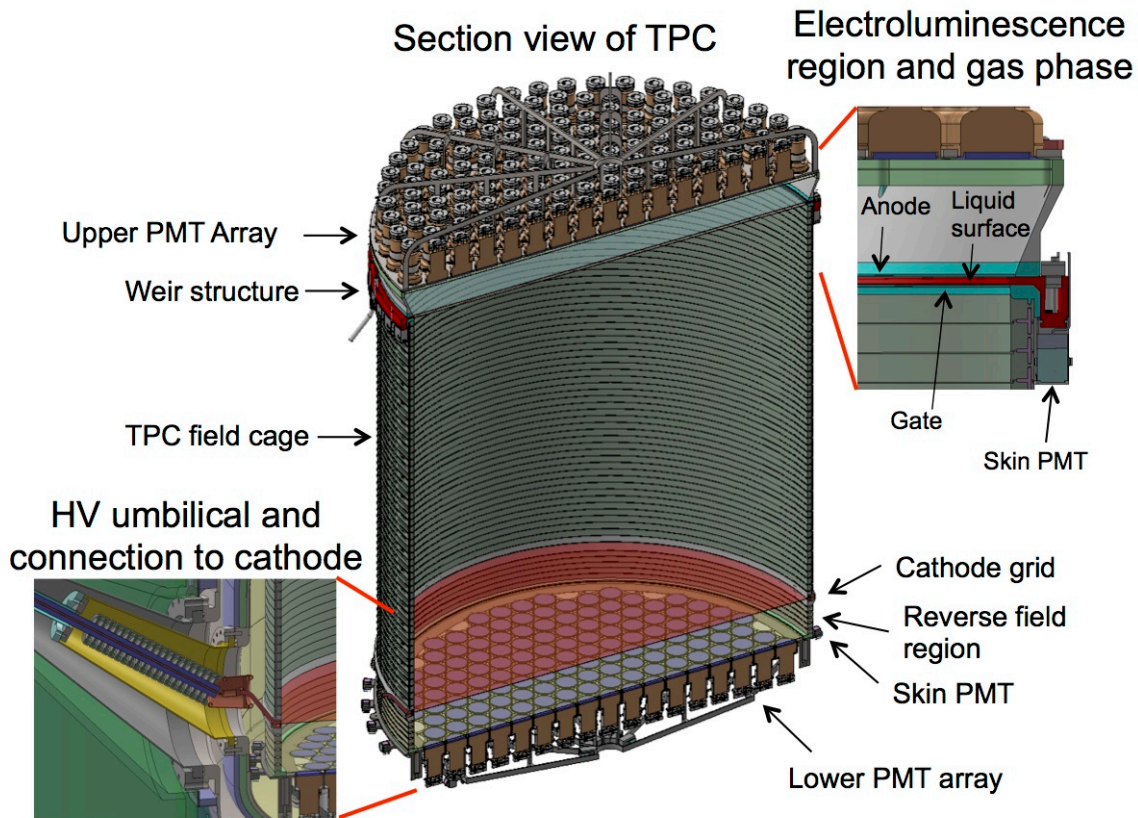


Figure 6.1.1. Schematic views of the Xe detector. The 7-tonne active region is contained in the TPC field cage between the cathode and gate electrodes, viewed by PMT arrays in the vapor and liquid phases. S2 signal generation occurs between the liquid surface and the anode (right inset). The HV connection to the cathode (left inset) uses a dedicated conduit leading from outside of the water tank. Below the TPC, the reverse-field region grades the cathode potential to low voltage at the bottom PMT grid. The lateral skin PMT readout is shown outside of the TPC field cage.

on the reverse-field region and cathode HV delivery system. An overview of the Xe detector system is shown in Figure 6.1.1.

By design, the structures surrounding the central Xe volume are as lightweight as possible for transparency to gammas and neutrons, and this also helps keep their total radioactivity low. The most challenging requirements on the intrinsic radioactivity (i.e., radioactivity per mass or area) are in the largest or most massive components — the PTFE walls and field-shaping rings, and the PMTs with their bases and cables. This section discusses the approach to obtaining the needed radioactivity levels for a number of these major items. However, the absolute level of radioactivity of everything in the detector system must be held at acceptable levels, so all components must be carefully selected and screened. We discuss the screening program that ensures this in Chapter 12.

6.2 Central TPC: Field Cage, PTFE Reflectors, and Grids

At the heart of the TPC are the field cage embedded in the reflective PTFE panels, and the grids. The grids and field cage create the set of electric fields that drift the electrons to create the S2 signal, and the highly reflective PTFE panels are essential to efficient measurement of the initial S1 scintillation signal.

6.2.1 Electric Field Design

The electric field configuration inside the TPC volume is made up of three distinct regions, described in detail in this section: (1) the drift region, (2) the extraction and electroluminescence region, and (3) the reverse-field region.

Cathode and Drift Region

The region between the cathode and gate contains the fiducial volume and is therefore one of the most important regions of the detector. This is where electrons are drifted up to the extraction region; hence, the electric field uniformity in this region has a major impact on the ability to fiducialize events in the detector. It is important that the electric field in this region be vertical and that the field lines are parallel to the surfaces of the cylindrical PTFE reflectors that set the outer boundaries of this drift region.

To produce a uniform electric field between the cathode and the gate electrodes, we use a set of 57 equally spaced field rings embedded in PTFE and connected by pairs of 1 GΩ HV resistors. The rings will be made from either C101 OFHC copper, or titanium from the same source as that used for the cryostat. The details of this design are shown in Fig. 6.2.1.1. The rings are T-shaped to help maintain the uniform field pattern needed within the TPC region by keeping the equipotential surfaces nearly normal to the inner surface of the PTFE rings.

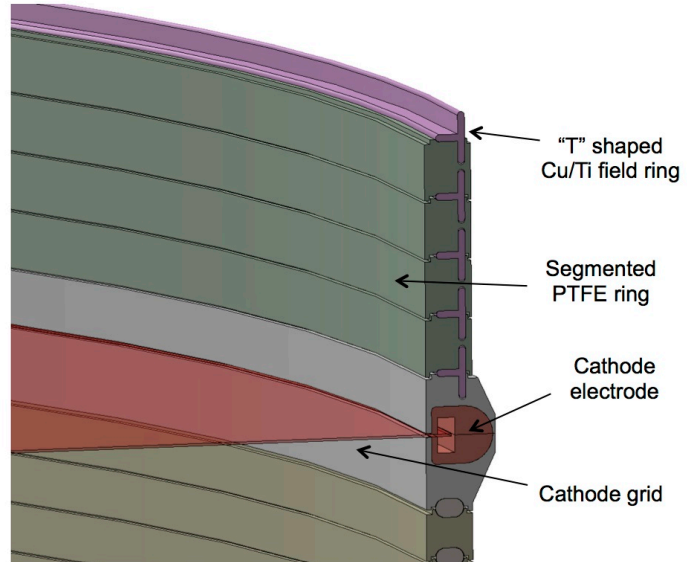


Figure 6.2.1.1. Cross section of the TPC walls in the drift region, with field-shaping structures embedded in the PTFE walls.

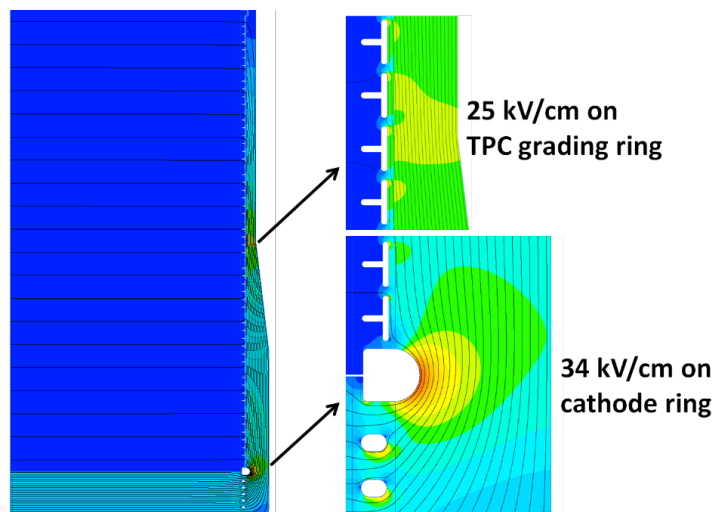


Figure 6.2.1.2. Field uniformity calculations for the bottom of the drift region and the reverse-field region of the TPC for LZ. High-field regions are yellow and orange while lower-field regions are green and blue. The right edge is the location of the grounded wall of the cryostat. The close-up views on the right show the maximum fields in the skin region on the cathode grid and field-shaping rings.

Figure 6.2.1.2 shows the calculated fields produced by this structure. The field-shaping rings are embedded in vertically and laterally segmented rings of PTFE that have been precision machined and then assembled in a stack to produce the completed field cage. The sharp difference in thermal contraction between PTFE and the metal field-shaping rings is accommodated by having these segmented pieces of PTFE slide laterally along the conducting rings when the detector is cooled. This approach is discussed in Section 6.2.3. The field cage structure will be mounted to the lower reverse-field region and lower PMT support, which in turn is supported from the bottom of the cryostat. The cathode grid will be constructed using a large circular 316 stainless steel (SS) frame that will hold two wire planes, each with 200-μm diameter ultrafinish SS wire planes oriented at 90° to one another, with the wires spaced every 1 cm in each

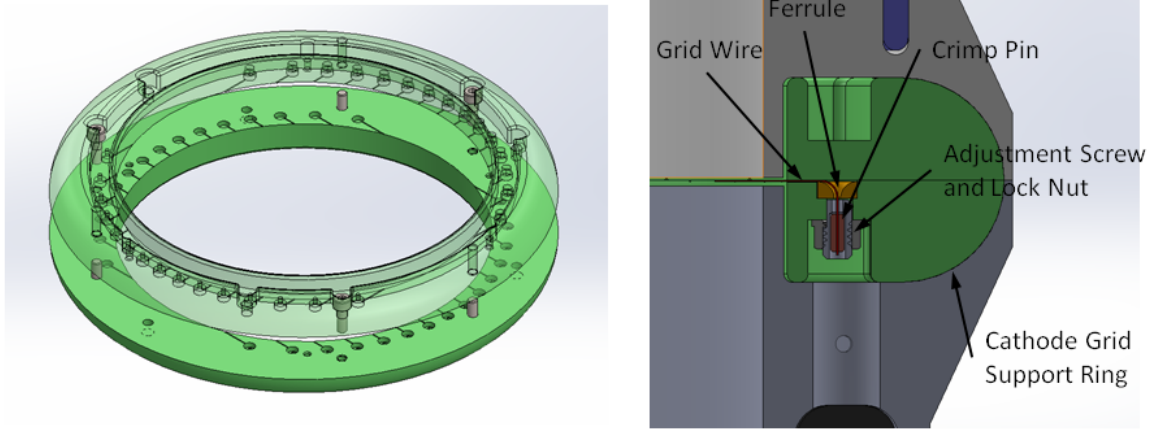


Figure 6.2.1.3. Left: View through the cathode grid ring for the first prototype assembly for Phase I system testing (see Section 6.10). The full LZ design will be essentially the same in all dimensions, apart from the overall diameter. The grid is composed of two planes of wire oriented at 90° to each other. In the figure, the top plane of the wire frame is transparent and the bottom plane is shown as solid. Right: The design of the wire-fixing mechanism that will be used to mechanically secure the wires in these grid frames.

plane. A large electrostatic attractive force exists between the cathode and bottom grids because of the high field in the reverse region; the tension on the wires in these grids must be large enough to limit distortions of the plane from this force. Setting a limit of ~ 2 mm deflection for 200 kV on the cathode, a 1 kg load is required in $200 \mu\text{m}$ O wires, which is well within the yield strength of available SS wires, but nonetheless represents an important mechanical requirement on the assembly. Note that the tension needed to minimize this overall deflection is larger than the minimum tension needed to prevent the well-known wire-to-wire “sawtooth” instability encountered in a single plane of wires in a wire chamber. This crossed set of wires will act as a large-opening wire mesh, with a 92% transparency (at normal incidence), providing the necessary field termination point at the cathode as well as allowing the lower PMTs a less obstructed view of the light produced in the TPC above. Two construction techniques for the grids are under consideration. One, based roughly on the method used by LUX, features a wire-crimping system with individually tensioned wires. This method has the advantage of all-metal construction, which minimizes outgassing or other contamination and provides good stability through temperature cycles. The other, which is optimal for a woven-mesh grid, is to capture the wires between two rings that are glued together. This method has the advantage of mechanical simplicity and having a smaller footprint than the crimp system. Details of the crimp method are shown in Figure 6.2.1.3. Small-diameter prototypes will be constructed and tested (see Section 6.10).

Reverse-Field Region

The reverse-field region between the cathode grid and the bottom PMT shield grid is one of the biggest challenges of constructing the LZ TPC because of the very high field involved. We must grade the cathode voltage from -100 kV to ground while keeping all surfaces in the fields in this region below the 50 kV/cm target described in Chapter 3. At the same time, we must try to keep this space as small as possible, both to reduce the amount of Xe in this region, and to reduce the rate of events that scatter in both the reverse-field region and the central TPC. Such events are a class of background that can mimic WIMP signals, but, as discussed in Chapter 3, have an acceptably low rate for the baseline design presented here. In the LUX detector, due to the much lower cathode voltages and the shorter drift region in the TPC, this was handled with a 4-cm spacing and no field grading between the cathode and PMT shield grids, along with a near-zero field region of 2 cm between the shield and the PMT front surfaces. For the LZ configuration, we have chosen a voltage-grading structure similar to that in the drift region.

This better defines the fields, and is a more robust approach to the more challenging LZ voltage requirements.

The current design, shown in detail in Figure 6.2.1.4, is composed of a stack of six PTFE “rings,” each ~2.5 cm high and embedded with a copper or titanium field-shaping ring. These conducting rings are placed near the outside wall of the PTFE rings to keep the field inside the TPC volume as uniform as possible above the PMTs while keeping the fields between the TPC region and the grounded outer cryostat below the required 50 kV/cm. The most recent calculated fields in this region can be seen in Figure 6.2.1.2. The smooth shape of these rings, compared with the T-shape in the drift field region, creates much lower surface fields on the rings, but results in a less-uniform field in the central LXe region. This is allowed because there is not a strong uniformity requirement in the reverse-field region. The voltages between each of the field rings are graded down from the cathode potential using a set of series resistors, similar to those used in the drift region, but we need 4 times the number of resistors between each ring to accomplish this stronger field grading.

The resistors in the reverse-field region are more challenging for radioactivity than those in the drift region because they are larger. The main radioactive challenge in electronic components is ceramic, which in all standard (non-“synthetic”) forms is very high in radioactivity. Our baseline plan, following LUX, is to use standard surface-mount resistor components that have the smallest ceramic mass for the required voltage rating. We are also considering custom fabrication of a film resistor on a base material made from synthetic quartz or sapphire, an approach that was successfully used by EXO [1].

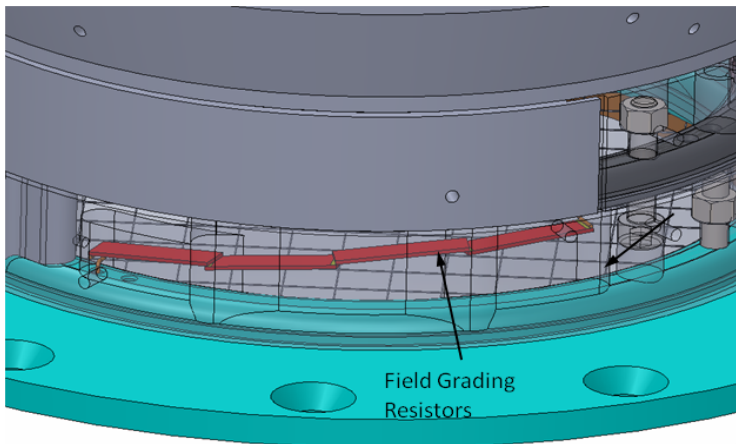


Figure 6.2.1.5. Placement of the four field-grading resistors in the reverse-field region, shown for the first system test prototype. The resistors are embedded inside the PTFE ring structure and attached to successive field-shaping rings.

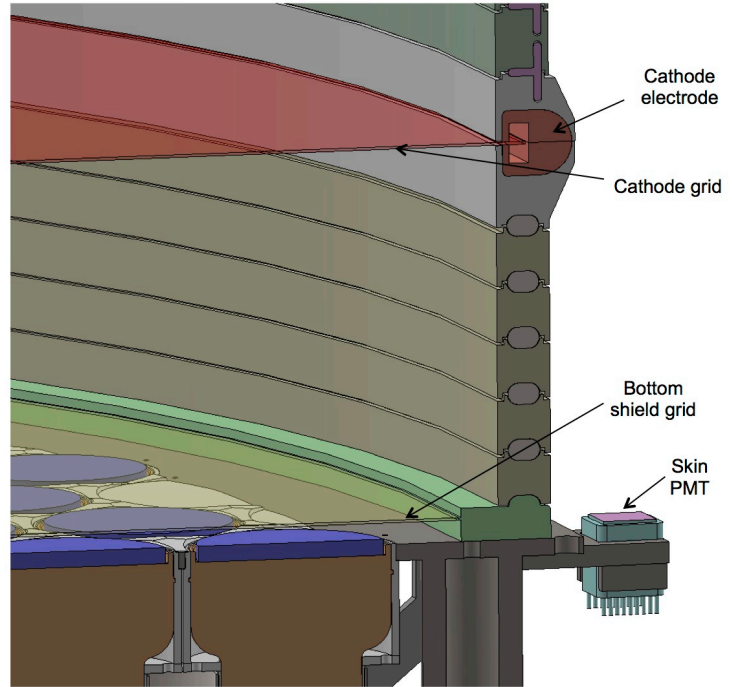


Figure 6.2.1.4. The reverse-field region, with the cathode (red) and bottom shield (green) grids visible, and the oval field-shaping rings used in this region.

We are also considering custom fabrication of a film resistor on a base material made from synthetic quartz or sapphire, an approach that was successfully used by EXO [1].

Figure 6.2.1.5 shows the current design and location of these grading resistors inside the PTFE spacers. The lowest PTFE “ring” will be attached to the top of the lower PMT shield grid and this grid will be spaced another 2 cm above the PMT surfaces, also using a PTFE spacer ring. This entire assembly will in turn be attached to the lower PMT support structure, which will then be fixed to the cryostat for final mechanical support. While extensive electrostatic

and mechanical studies of this region have been carried out, we consider this design to be preliminary, in particular until it has been tested as one of the first elements of the system test program described later.

Electroluminescence Region

The design of region above the gate grid, where the electrons are extracted from the liquid and create the S2 signals before they are collected on the anode grid, presents several challenges. The fields are high; the optimization of the grids to create the S2 signal requires care, as is discussed in detail in Section 6.6; the mechanics of having gate and anode grids with very low deformation from the large electric fields is challenging; both the weir structure (Section 6.8) and skin PMTs (Section 6.7) must be accommodated in a tight space; and the overall structure must maintain a very low level of distortion in the rings supporting the anode and gate grids, so that a parallel arrangement of grids and liquid surface can be obtained (tip-tilt adjustment of the detector to assure parallelism of grids and liquid surface is discussed in Chapter 8). A close-up view of this region is shown in Figure 6.2.1.6.

The field in the liquid above the gate must be significantly stronger than the field in the drift region, because a ~ 5 -kV/cm “extraction” field is needed in order to give the electrons sufficient kinetic energy to overcome an energy barrier at the liquid surface and be extracted into the gas phase with near-unity probability. Once electrons enter the gas phase, where the field is approximately twice as strong due to the lower dielectric constant there ($\epsilon_{r,liq}=1.96$), they are accelerated and produce electroluminescence photons in the 5-mm drift distance until they are collected on the anode grid. The photon yield is ~ 550 photons per emitted electron at 1.6-bar operating pressure, with 10 kV/cm in the gas. For these operating conditions, the electron transit time to the anode is $\sim 0.7 \mu\text{s}$, which, along with diffusion while the electrons drift in the liquid, determines the width of the S2 pulse.

The gate electrode decouples the field applied to the drift region — which tends to be limited to ~ 1 kV/cm or lower due to the length of the chamber — from the ~ 5 -kV/cm extraction field above it. The gate grid is assembled onto a circular SS frame, with a single wire plane stretched and fixed in a similar fashion to the cathode grid described previously. It will employ 100- μm ultrafinish SS wires wound with

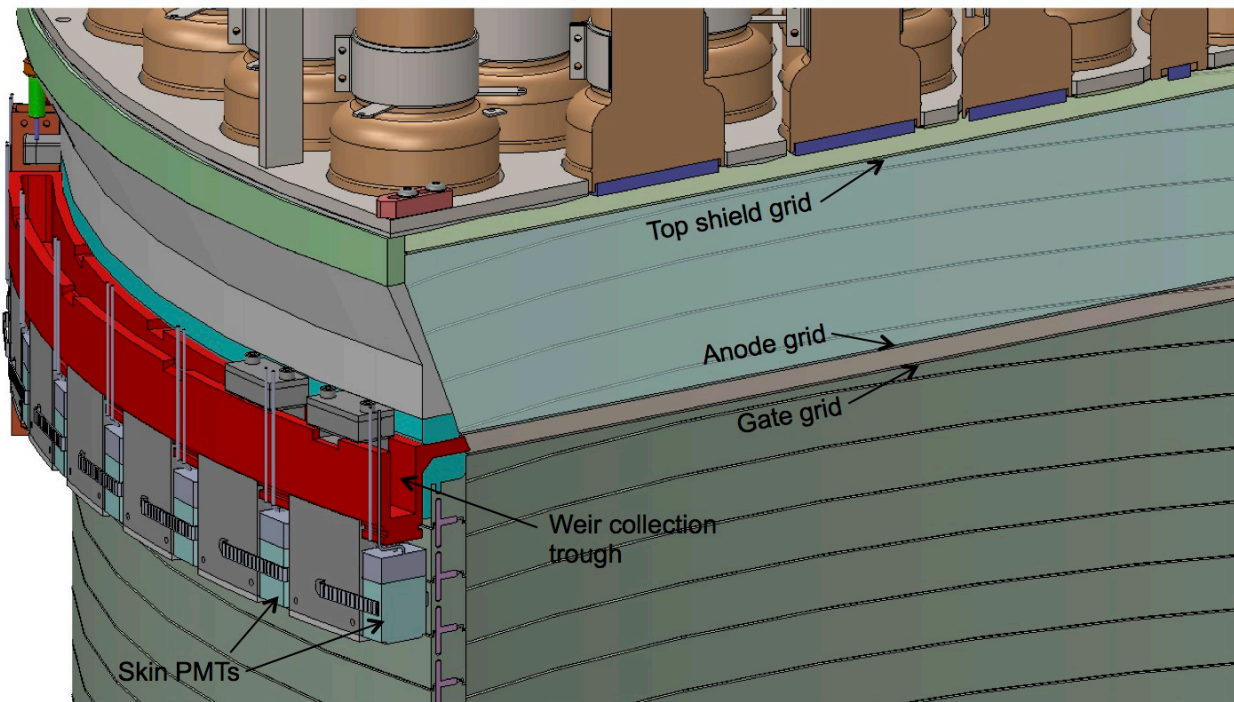


Figure 6.2.1.6. The electroluminescence region, with the gate, anode, and top shield grids shown, along with the weir, and top skin PMTs.

a spacing of 5.0 mm, with the wires fixed on this frame after stretching using the staking system described for use on the cathode. This choice of wire and spacing results in an optical obscuration of only 2.5%, while the transparency for drifting electrons is approximately 100%. The upper element of this electrode assembly is the anode, located nominally 5 mm above the liquid at the top of the TPC.

Because the S2 signal develops as the electrons drift from the liquid surface to the anode electrode, it is essential to minimize the variance of S2 photon production for different electron emission points, as this relates directly to the energy resolution achieved in the S2 channel (and hence to discrimination). Firstly, the tension on the both the gate and anode wires must be significant in order to minimize sagging as well as electrostatic deflection, ensuring a relatively uniform electroluminescence response across the entire surface of the detector. A small deflection can be calibrated to first order by mapping the width of S2 pulses in (x,y) using calibration data, since this is proportional to the transit time in the gas, but our goal is to keep deflection at the center of both grids to <1 mm. This is feasible in terms of wire strength, but will require the entire gate and anode grid assembly to have high mechanical integrity. That stability will be aided by robust coupling of those grids to the upper PMT array, as indicated in Figure 6.2.1.6. Secondly, to minimize S2 variability on the scale of individual wires, these anodes tend to be constructed from densely packed fine wires, chemically etched meshes, or woven meshes. Our baseline design, based on LUX, uses a woven mesh of 30- μm wires on a 250- μm pitch. Figure 6.2.1.7 shows a prototype anode using a stretched mesh employed in LUX construction. The optimization of the design for S2 signal production is further discussed in Section 6.6.



Figure 6.2.1.7. A 1.16-m-diameter stretched prototype of the LZ anode grid.

A final element in this region is the upper PMT shield grid. The function of this electrode is to match the potentials from the TPC to those of the photocathode of the phototubes. This grid will be located about 4 cm above the anode and about 1 cm below the PMT windows. It will be constructed once again using a circular SS frame that we will stretch 100- μm ultrafinish SS wires at a pitch of 1 cm, similar to the other individual wire grids used in the TPC.

6.2.2 VUV Reflectors

Based on the experience of the LUX experiment in optimizing light collection within the TPC volume through the use of high-UV-reflectivity PTFE panels, we intend to use the same material, albeit in a slightly different configuration to maintain this same high reflectivity within the LZ TPC and skin regions. Our plan is to use machined “rings” of high-purity PTFE approximately 2 cm thick and 2.5 cm tall to form the inner reflecting surface in the TPC region as well as the outer reflecting surface between the TPC and the cryostat wall, which itself will have a few-mm-thick segmented lining of PTFE. As mentioned earlier, the reverse-field region will be composed of six such rings stacked on one another, and the drift field region will be formed from a stack of 57 such “rings” where the field-shaping electrodes are embedded inside the PTFE. This configuration provides the support for necessary electrode structure needed to produce a uniform drift field.

The radioactivity of PTFE must be held low both because of direct gamma production and, more importantly, neutron production from (alpha,n) reactions on F from alpha decays in the U and Th chains. The raw precursor material for PTFE structural material is a powder form produced by DuPont and a few other suppliers, and is expected to be extremely low in radioactivity because of the gas-phase process

used to produce it. A large number of smaller manufacturers produce structural shapes from these powders, and the final material can be very low in radioactivity if there is sufficient care in controlling contamination (e.g., from dust) in this second manufacturing step. We assume numbers equal to the limits achieved by EXO [2] working with a company with which we are in contact (see Chapter 12 for further discussion). These are 0.01, 0.002, and 0.06 mBq/kg in U, Th, and K, for which the gamma background is negligible and neutron backgrounds are somewhat subdominant to the assumptions for the PMTs and much below conservative Ti estimates.

6.2.3 Thermal Considerations

Given that the inner detector region is composed of PTFE, SS, and copper/titanium pieces, attention must be given to the issue of differential thermal contraction as the detector is cooled to LXe temperatures. The PTFE that makes up the majority of the surface area of the TPC is expected to shrink by $\sim 1.7\%$ linearly, or about 7.6 cm in circumference and 1 cm in TPC radius when cooled from room temperature to ~ 170 K. Stainless steel, by contrast, contracts only $\sim 0.2\%$ over the same temperature range, and titanium even less. We have chosen to cope with these differences by constructing the metallic field cage rings as solid assemblies, while the PTFE rings are segmented both horizontally (i.e., into rings) and vertically, so that each ring is itself composed of several segments. These latter segments contract and slide circumferentially along the solid metal field cage rings. In this way, the overall diameter of the TPC is determined by the metal field cage rings, and thus undergoes a relatively small thermal contraction. As the PTFE contracts, the seams between the segments open, but the design has overhangs such that there will continue to be a reflecting surface in the exposed gaps. In the vertical direction, the dimension of the field cage is determined by the PTFE panels, and there is an overall height (top PMT array to bottom PMT array) contraction of about ~ 2.6 cm. To minimize the movement in the critical region where the HV connection to the cathode is made (discussed in Section 6.3), we have chosen to support the entire TPC assembly from the bottom PMT array, which will be connected to the cryostat vessel. This means that the top PMT array will contract downward, increasing the Xe gas-filled region in the top dome.

6.2.4 Field Uniformity

In LUX it was observed that field lines at the side edges of the TPC, particularly near the top and bottom, are not fully parallel to the PTFE surfaces. We have come to understand this as being intrinsic to its design: The overall fields resulting from the grids and field cage structure were designed using 2-D electrostatics calculations that treated the grids as continuous conducting sheets. It is well known [3,4] that the 3-D stretched-wire grids have a “transparency” such that the bulk electric fields are somewhat ($O(10\%)$) different than the values calculated assuming the grids are conducting planes, and this effect was taken into account in establishing the operating fields. But a subtler additional effect happens at the top and bottom of the TPC cylinder, where the transparency of the grids causes some bleed-through of the concentrated fields that terminate on the vessel and other grounded structures just outside the main part of the TPC. A more complete calculation using transparent grids reproduces the observed pattern in LUX. Such an effect was in fact previously observed in XENON100 and understood as described above [5].

In LUX, this effect caused electrons at the bottom edge of the detector to deflect ~ 2 -3 cm inward as they followed distorted field lines. This did not pose a fundamental problem for the science data, since the effect could be readily corrected for in analysis. Nonetheless, we will seek to better control the fields in LZ. Based on preliminary electrostatic calculations, we believe we can mitigate this effect by adjusting the values of the last few resistors at the top and bottom of the field cage, and possibly modify the geometry of the electrodes in this area. Another design change over LUX is the vertically segmented design of the PTFE field cage walls. The essentially uninterrupted PTFE surfaces of the field cage are necessary for good light collection, but not ideal from the point of view of good high-voltage design practice, because insulating surfaces can at least in principle accumulate charge that distorts fields. LUX was constructed of vertically continuous slabs of PTFE, whereas the 2.5-cm-tall segments in LZ provide much shorter paths to the conducting field rings from any location on the PTFE walls.

6.3 Cathode HV Delivery System

6.3.1 Cathode HV Requirements

The cathode HV for LZ is a critical performance parameter that will directly affect the science reach of the instrument because of its impact on ER rejection. Introduction of HV into the Xe space is challenging because of possible charge buildup and sparking, and also because high-field regions can produce electroluminescence that blinds the detector to the flashes of light produced by WIMP interactions.

The LZ operational and design voltages were determined through a combination of task-force activity, evaluation of dark-matter sensitivity, and project cost and risk. Between December 2012 and April 2013, a dedicated LZ task force of 10 engineers and scientists examined the various design ideas and critically evaluated their technical feasibility, with the scope covering the grids, portions of field cage, internal connections, and the cathode feedthrough. The task force culminated in a 46-page report [6]. The operational cathode HV for LZ will be -100 kV, so as to generate a ~ 700 V/cm drift field. At this drift field, an ER rejection efficiency of 99.5% is expected at 50% NR acceptance, as demonstrated in previous two-phase Xe detectors and modeled through the Noble Element Simulation Technique (NEST) simulation package. The LZ design cathode HV goal is -200 kV; all subsystems in LZ will be designed to withstand a -200 kV cathode voltage to help ensure that a -100 kV operational voltage can be met.

6.3.2 Cathode HV System Overview

An overview schematic of the cathode HV system is shown in Figure 6.3.2.1. The baseline LZ design places the cathode HV feedthrough (from air into Xe space) outside the shield at room temperature, at the end of a long, vacuum-insulated, Xe-filled umbilical. With the dominant cable material being polyethylene, Rn emanation is minimized. Polyethylene is known to be a safe material in LXe, mitigating concerns about emanation of electronegative contaminants. With the feedthrough at room temperature and far away from the active LXe, there are no concerns of thermal contraction compromising a leak-tight seal to the Xe space, and no concerns about feedthrough radioactivity. A feedthrough at the warm end of the umbilical allows a commercial polyethylene-insulated cable to pass from a commercial power supply,

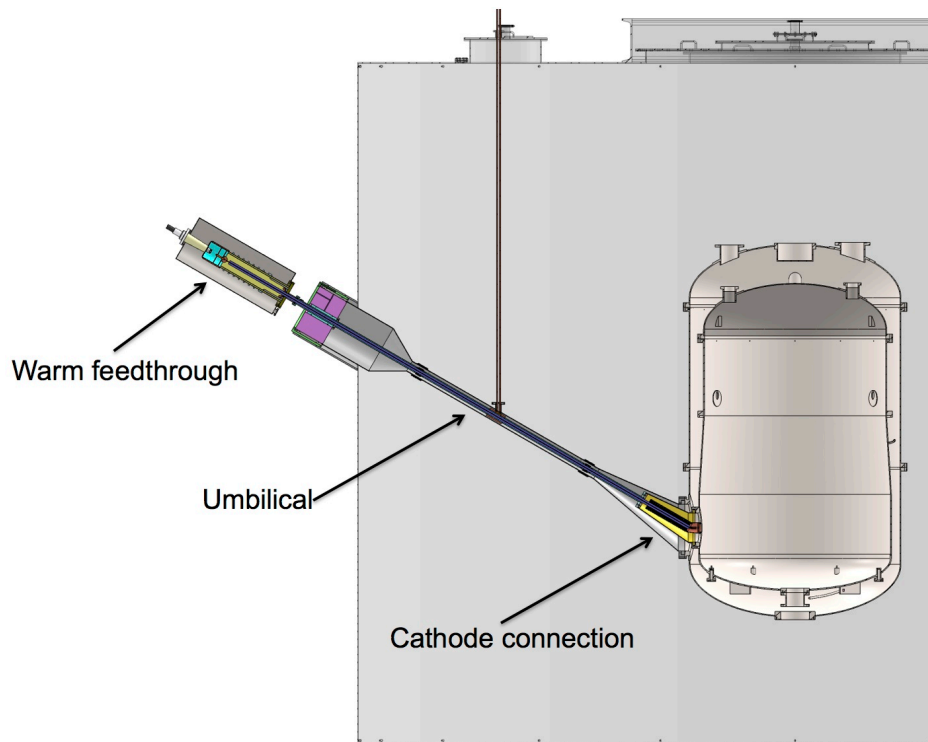


Figure 6.3.2.1. Overview of the cathode HV system.

through an HV epoxy plug, and into the gaseous Xe. The cable then travels through the center of the umbilical and routes the HV through LXe and to a field-graded connection to the cathode. A smaller version of this feedthrough is installed in LUX, and was successfully tested up to 100 kV in gaseous argon before installation. A prototype warm feedthrough has been successfully tested at Yale up to 200 kV, with the cable terminated in transformer oil.

6.3.3 Cathode HV Supply and Cable Connection

The maximum design voltage for the cathode grid is -200 kV. The cathode grid power supply is an XRV series power supply rated at -225 kV from Spellman High Voltage and is a standard model for medical and industrial X-ray applications. Several modifications to the standard model limit the maximum current to <1 mA, enhance the resolution of the internal current monitor for accurate measurement of the load current, and reduce the stored energy in the internal capacitance to limit available fault energy. The power supply output connector is a standard R28 connector from Essex X-ray and is rated for 225 kV. The output cable is type Q HV cable from Parker Medical that has an internal resistance of 75 ohms/ft to further limit fault current and energy in the event of an HV breakdown at the load. This cable is terminated into a commercial vacuum feedthrough from Parker Medical (H1827P03) that is rated at 220 kV. By leveraging these commercially available components designed for medical and industrial X-ray applications, the design of the HV generation and delivery system into the warm feedthrough is safe, reliable, cost-effective, and readily available.

6.3.4 Cathode HV Feedthrough

The warm cathode HV feedthrough, shown in Figure 6.3.4.1, supplies negative HV to the cathode of the LZ detector. The feedthrough is a specialized termination of an HV polyethylene cable, Dielectric Sciences model 2077, which is rated for 300-kV DC operation. The far warm end of this cable is symmetrically encased in epoxy plastic, which forms a vacuum seal to the cable. This epoxy also forms a vacuum seal to fiberglass tubing that is in turn sealed to a standard 8-inch conflat vacuum flange. This combination forms a helium-leak-tight seal between the conflat and the cable, while confining all strong electric fields within the epoxy plastic. The cable emerges from the conflat-flanged end of the feedthrough, within the Xe space of the detector, while at the opposite end of the termination a metal sphere embedded in the epoxy acts as a terminal for the HV connection. The other side of the sphere is housed in vacuum, where a connection is made to a commercial feedthrough leading to a commercial HV

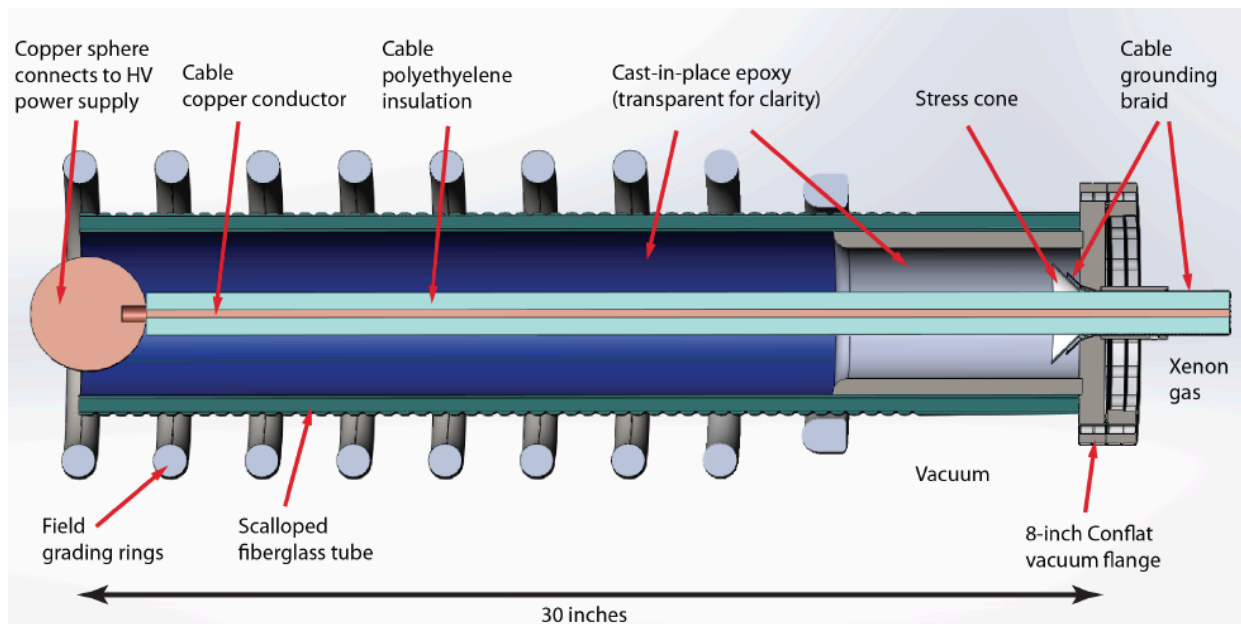


Figure 6.3.4.1. Warm feedthrough detail for the HV connection to the cathode.

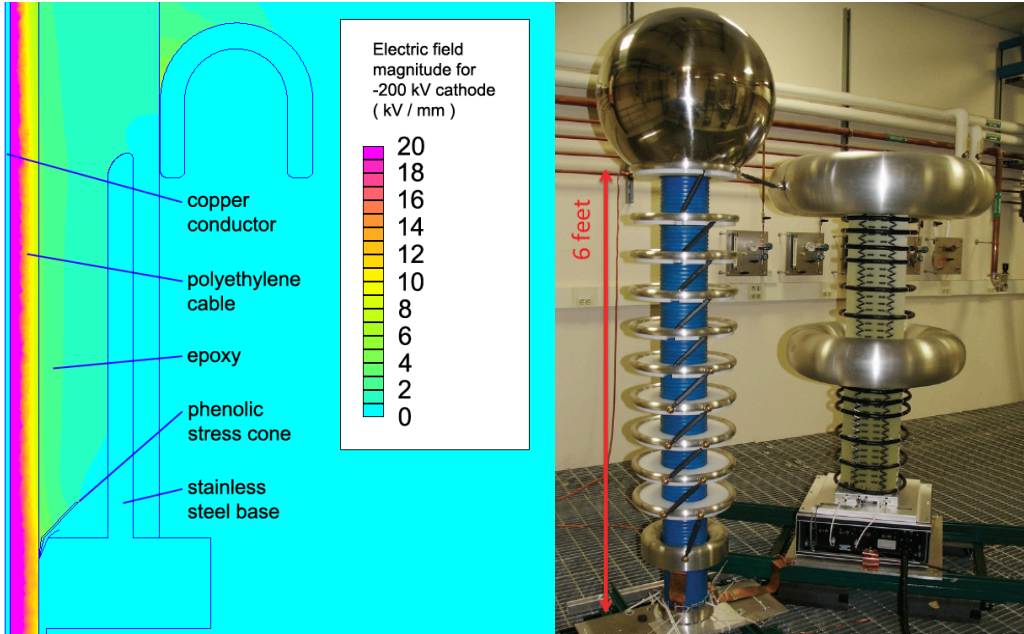


Figure 6.3.4.2. Left: Electric field simulation of warm feedthrough, at the critical region where the polyethylene cable passes through the flange dividing vacuum space from Xe space (this is on the right end of the assembly in Figure 6.3.4.1). Right: Photograph of warm feedthrough (blue structure on right), under test at Yale.

power supply. An electric field simulation of the warm feedthrough and photograph of a prototype warm feedthrough are shown in Figure 6.3.4.2.

6.3.5 Cathode HV Umbilical

The cathode HV umbilical, shown in Figure 6.3.5.1, is designed to carry the Dielectric Sciences HV cable from the warm feedthrough to the cathode of the detector. It is formed of a nested pair of tubes that protrude from the side of the detector at about the height of the cathode. These rise upward in at an angle of 30° from the horizontal and penetrate the water-tank side wall at approximately 3/4 of the height of the tank. The inner tube of the umbilical is connected to the Xe space and is joined to a protrusion from the inner vessel of the detector by a short bellows. The outer tube of the umbilical contains vacuum and is similarly connected to the outer vessel of the detector. The outside of the outer tube is immersed in the water of the tank. The evacuated space between the tubes contains super-insulation reflective wrap and acts to thermally isolate the Xe space from the water. This allows

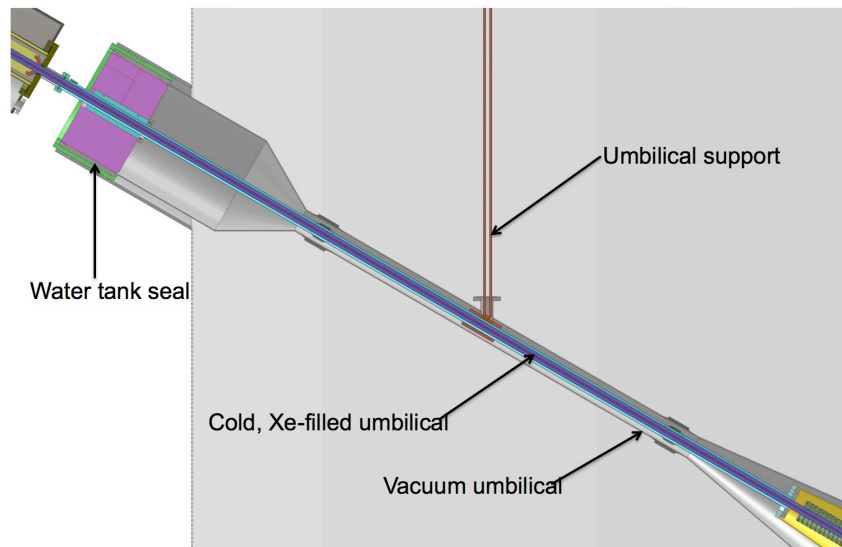


Figure 6.3.5.1. Detail of the HV umbilical that spans between the HV cable at room temperature on the left, and the connection to the cold cathode grid on the right.

LXe to fill the inner tube of the umbilical until it reaches a height equal to the level of the Xe surface inside the detector. Thus, the lower part of the umbilical is filled with LXe, while the upper part contains Xe gas. The long length of LXe is necessary to accommodate the field-grading region of the HV cable. A port near the high end of the umbilical connects to the Xe circulation system to allow control over the flow of Xe through the umbilical. Finally, the high end of the umbilical connects to the warm HV feedthrough. The umbilical is heavy and is supported from a structure standing on the floor of the water tank.

6.3.6 Spark and Discharge Mitigation

The field-grading structure at the cold end of the HV cable, shown in Figure 6.3.6.1, allows for the ground braid of the cable to terminate while the polyethylene insulation and conductive center of the cable continue. This structure is long in order to minimize the electric field parallel to the surface of the cable. The cable is surrounded by 20 field rings made of conductive plastic. These rings enclose coil springs that grip the cable circumferentially and provide electrical contact to its surface. The field rings are connected in series by small resistors to establish a uniform voltage grading between them. The highest potential ring (lower right of figure) is connected to the center conductor of the cable, while the lowest potential ring (upper left of figure) is connected to the cable ground braid. The surfaces of the rings are heavily rounded, and the resistors are nested between them. This minimizes the field within the LXe that surrounds the grading structure and separates it from the grounded wall of the inner tube of the umbilical. The grading ring structure is supported entirely by the HV cable, so there is no need for a “stand-off” to the grounded wall of the umbilical. The entire grading structure is immersed within the LXe; all sections of the cable within Xe gas have an intact ground shield. An alternative design being considered has a more gradual departure of the cable ground braid from the cable surface. This further reduces the field within the LXe near the cable surface.

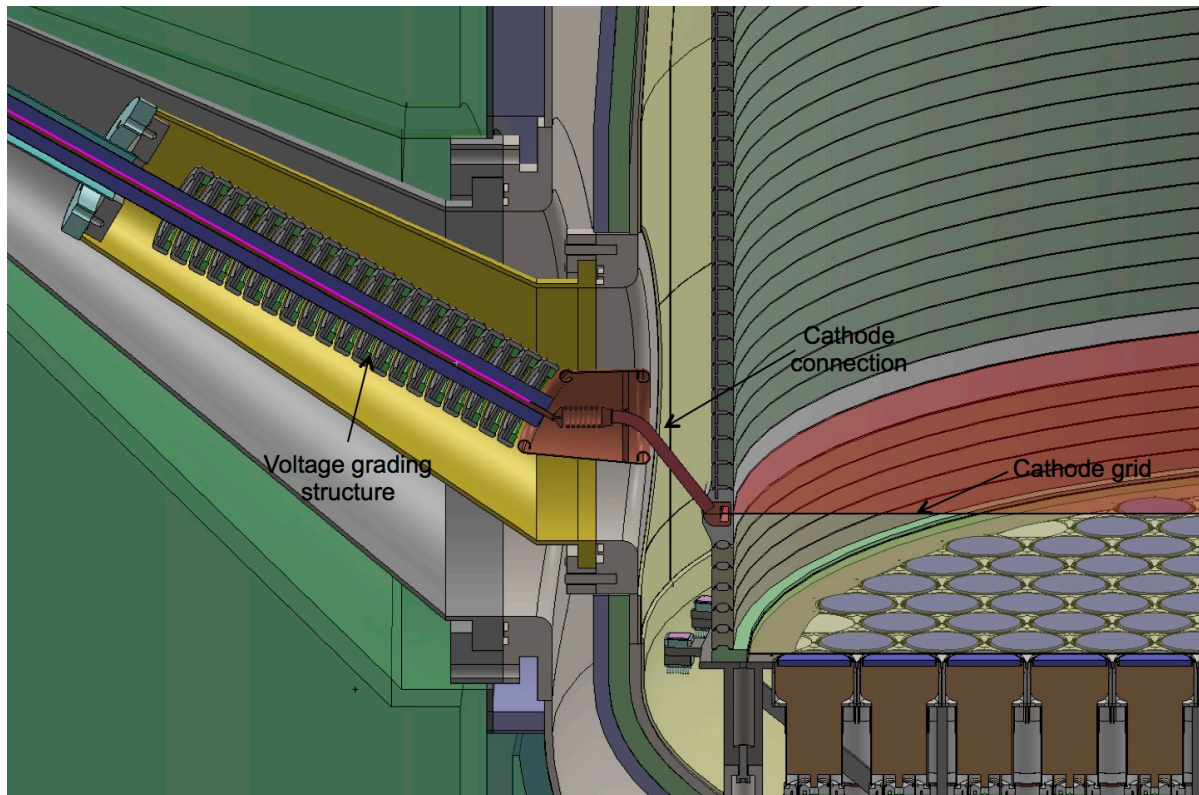


Figure 6.3.6.1. Schematic of the flexible HV connection to the cathode grid, showing details of the field-grading structures on the incoming HV cable required to keep the fields in the LXe below 50 kV/cm.

6.3.7 HV Connection to the Cathode

A schematic of the HV connection to the cathode is also shown in Figure 6.3.6.1. Because the TPC (including the cathode grid) is supported from the bottom of the vessel, the cathode grid moves down approximately 2 mm as the PTFE TPC components contract when the system is brought from room temperature to operating temperature (~172 K). To account for this movement, a compliant spring connection between the end of the HV cable and the hardware is fixed to the cathode grid ring. The hardware that extends radially from the cathode grid ring is designed to be stiff with minimal weight, as it is a cantilevered load, and to provide sufficient electric field shaping to shield the field enhancements of the small connection components.

6.3.8 HV Safety Issues

The combined stored energy from the cathode power supply output capacitance, output cable capacitance, warm feedthrough and umbilical capacitance, and TPC capacitance is approximately 8 J at the 100-kV operating voltage, and is classified as yellow 3.2C [7]. This hazard class indicates that injury or death could occur by contact (shock). To mitigate this shock hazard, engineering controls are required for operation and administrative controls are required for electrical work. Specific lockout/tagout and grounding procedures will be implemented for various operations such as unplugging the output cable and accessing the internals of the warm feedthrough, umbilical, and the TPC. Each worker who is authorized to perform these tasks will have energized work training and specific HV, high-current, and high-power safety training.

6.4 Photomultiplier Tubes

To reach the performance specifications described previously, the Xe detector is equipped with top and bottom arrays of 3-inch-diameter PMTs (Hamamatsu R11410-22) to view the active region of the TPC, and top and bottom rings of smaller, 1-inch-square PMTs (R8520) to view the scintillation light emitted in the Xe skin — the region outside the TPC and inside the cryostat inner vessel. Both types of PMT have been developed to meet important performance requirements, including good spectral response in the VUV, good single-photoelectron definition, low dark noise, and the ability to operate at LXe temperature, in addition to having ultralow levels of radioactivity of ~mBq/unit in U/Th. This section describes in detail the properties and deployment of the PMT for the TPC and skin. Subsequent sections discuss the design and optimization of S1, S2, and skin light signals.

The LZ Collaboration has been pursuing the development of ultralow-background PMTs tailored specifically for use in LXe with a radioactivity goal for U/Th of 1/1 mBq per unit and QE >30% at 178 nm wavelength [8]. The LZ experiment configuration requires ~500 3-inch PMTs, and double that number if 2-inch-diameter tubes were used instead. Because of its outstanding radioactivity performance, the 3-inch Hamamatsu R11410-22 model has been adopted; this tube contains ~1,000 times less radioactivity than a standard off-the-shelf item and is the result of our coordinated development with the manufacturer and a very rigorous screening campaign of subcomponents before the items are even manufactured.

The dynode optics in the R11410 are electrically identical to those used in LUX (2-inch R8778), exhibiting similar gain and single photoelectron response. The distribution of QE at 178 nm is also compatible with that of the previous model (26% typical). The photocathode diameter is 64 mm. This tube has 12 dynodes and provides a gain of 5×10^6 at 1,500 V bias voltage. The PMTs are assembled to passive voltage divider bases and will be negatively biased so that the signal can be collected by directly coupling the amplifier electronics at near-ground potential. Very high peak-to-valley ratios >2 are obtained for the single photoelectron response, which is a key parameter to ensure high detection efficiency for the smallest S1 signals that are composed of single photoelectrons appearing in multiple PMTs.

Besides good VUV sensitivity, these quartz-windowed PMTs are designed to be operated at LXe temperature featuring a special low-temperature bialkali photocathode with low surface resistivity. This obviates the need for metallic underlayers or conductive fingers [9]. In any case, we will confirm correct operation for every unit through a comprehensive low-temperature test program to confirm optical and electrical performance during and after thermal cycling.

6.4.1 PMT Radioactivity Specifications and Radioassay Program

Due to their complexity, total mass (~100 kg), and proximity to the active volume, the Xe-space PMTs are a significant source of radioactivity background in LZ. For this reason, they will be subject to a thorough screening campaign using HPGe detectors (see Chapter 12). Screening of fabrication materials and subcomponents will take place prior to PMT manufacture, and every assembled PMT will again be screened after delivery from Hamamatsu.

The 3-inch R11410 has been delivered in part through a 4-year NSF S4 development program by Brown University with Hamamatsu, which achieved unprecedented radioactivity performance compared with previous generation tubes [10]. Further analysis of results from the screening of 25 of the R11410-20 first-generation model of this series is shown in Table 6.4.1.1. The ^{60}Co levels have been reduced in R11410 production that followed these earlier prototypes. Measurement sensitivity on early-chain ^{238}U activity is being further improved using new detectors as discussed in Chapter 12. That same model PMT has also been advanced by other collaborations, notably XENON1T with variant R11410-21.

Comprehensive radioactive screening results for 216 of these PMTs are publicly available [11] as shown in Table 6.4.1.1. Results from the screening programs are in broad agreement. LZ intends to procure the most recent R11410-22 version of these tubes.

We use the values in Table 6.4.1.1 to establish our background levels in simulations, as reported in Chapter 12. The 3-inch PMTs account for 1.2 ER events in a 5.6T fiducial volume in 1,000 days, before discrimination, and 0.2 NR events. They are a significant source of NR events among internal detector components, providing neutrons both through spontaneous fission (majority component) and (alpha,n) reactions in the PMT materials. As discussed in Chapter 12, spontaneous fission neutrons can be vetoed even more effectively than those from (alpha,n) reactions; however this has not yet been taken into account in the current NR estimate (see the discussion in Table 12.2.2). In addition, as also discussed in Chapter 12, new detectors are improving screening sensitivities to ^{238}U , so we expect to further improve the errors/upper limits on the presence of the dominant spontaneous fission emitter.

The 1-inch R8520 PMTs used in the skin detector have radioactivity levels that are well understood thanks to their wide use in past detectors. Nevertheless, we will adopt for them the same screening procedures as for the larger R11410 as described above. The contribution of the 180 skin PMTs to the background of the instrument is subdominant (see Table 12.2.2), given their comparable specific activity but more peripheral location and smaller number.

Table 6.4.1.1. Radioactivity summary per unit for LZ skin detector PMTs (R8520) from [12], for LUX PMTs (R8778) [8], and for LZ TPC PMTs (R11410) based on 25 early-production R11410-20 LZ PMTs. Values for the R11410-21 model studied extensively in [8] are also shown. Average activities per PMT are quoted per parent decay. Errors are 1σ and upper limits are 90% CL.

PMT	^{238}U (early) mBq	^{226}Ra (late) mBq	^{232}Th mBq	^{40}K mBq	^{60}Co mBq
R8520 (1")	< 1.39	0.12 ± 0.01	0.11 ± 0.01	7.6 ± 0.9	0.55 ± 0.04
R8778 (2")	< 3.0	9.5 ± 0.6	2.7 ± 0.3	66 ± 2	2.6 ± 0.1
R11410-20 (3")	< 26	1.1 ± 0.4	1.5 ± 0.5	25 ± 4	2.1 ± 0.2
R11410-21 (3")	< 12.9	0.52 ± 0.1	0.39 ± 0.1	11.9 ± 0.2	0.74 ± 0.1

6.4.2 PMT Bases and Cabling

Individual passive voltage-divider bases and two coaxial cables (for HV bias and signal) are attached to each PMT. Given their locations, these components are also under detailed scrutiny and selection as part of the radioactivity and radon-emanation screening programs. The latter is a critical consideration for the ~1,400 cables that terminate in the feedthroughs at the warm end. Sleeved and sleeveless candidate cables are presently being assayed for this purpose.

The voltage-divider bases are made from thick polyimide PCB (Cirlex) with surface-mounted passive components. Cirlex is an excellent material for this purpose, having very high dielectric strength, a low thermal expansion coefficient, high tensile strength, and low internal stress. The voltage-divider circuits are as recommended by Hamamatsu. High-resistance chains are used for low power dissipation in the LXe (24 mW/unit), which is essential to prevent bubbling and to have minimal impact on the thermal design of the detector. Charge supply capacitors are added to the last few dynodes to improve linearity.

The radioactivity performance of the PMT bases is of special concern, both from the point of view of neutron/gamma emission and from radon emanation. Although Cirlex is intrinsically a radio-clean material, the discrete components make more significant U/Th contributions, in spite of the small masses employed. Of particular concern are the ceramic (barium titanate) capacitors, the high concentration of ^{210}Pb commonly found in resistors, and the spring materials used within pin receptacles to connect to the PMTs and the cables. The current program for gamma-ray screening of the passive components for the bases has already identified a design that delivers lower gamma-ray activity than the PMTs. Our target for the bases is to keep these components at one-third of the PMT radioactivity or less. We will continue to survey potential components to further reduce this contribution prior to finalizing component choice as production nears.

The PMT signals and HV supplies are carried separately between the PMT bases and the warm breakout interface by low-radioactivity coax cables. The baseline design is to use Gore 3007 Coax with no outer jacket, the same cable that was used in this role for LUX. The 50-ohm characteristic impedance cable uses an AWG 30 silver-plated, Cu-clad steel, surrounded by an AWG 40 SS braid.

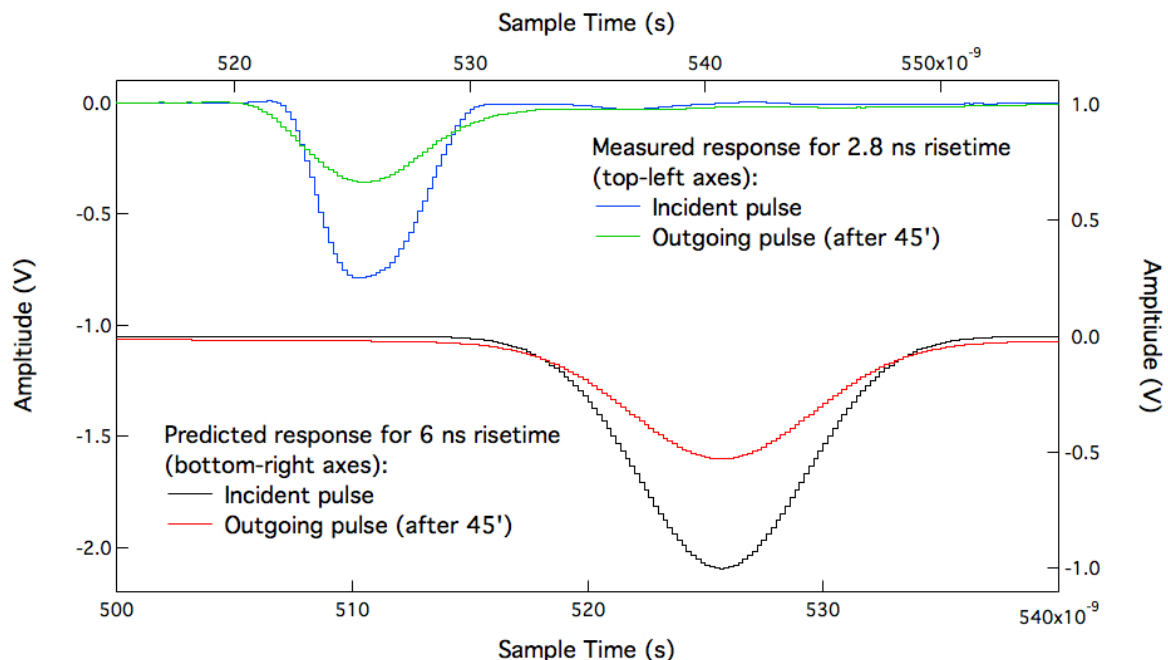


Figure 6.4.2.1. Measured signal attenuation from 13.7 m (45 ft) of Gore 3007 Coax in response to 2.8 ns rise-time pulses, and calculated response for 6-ns rise-time signals, which is approximately the anode pulse rise time for the R11410 PMTs.

The cables from the PMTs associated with the upper and lower parts of the TPC are housed in separate conduits, so that no cabling is routed through the side skin region. This could interfere with the ability to hold a high voltage on the cathode and it would degrade the light collection efficiency from the skin region.

The lengths of typical top and bottom cables are 12.8 m and 11.6 m, respectively. The upper routing consists of 672 cables for 247 TPC and 60 skin-veto PMTs, plus internal monitoring sensors. The lower routing consists of 744 cables for 241 TPC and 60 (side) and 60 (dome) skin veto PMTs, plus sensors. Twelve cables included in this count will be run down both paths as dummies for electrical troubleshooting. The total heat load calculated from the cables is less than 6 W, which is a subdominant contribution to the thermal model. A screening program has been initiated to measure the Rn emanation from the baseline cabling, as well as possible alternatives, to ensure that the finally selected cable will meet the overall Rn requirements discussed in Chapter 12. The Rn emanation from the cable is expected to be dominated by the warm region, which is 8 m in length for the upper routing, and 1 m for the lower routing. Emanation from the feedthroughs (which were previously used in the LUX experiment) will also be measured.

The Gore 3007 cable has been tested and shown to support 2 kV, comfortably meeting the HV requirements of all PMTs. The signal characteristics for a 13.7-m length are shown in Figure 6.4.2.1. For a 6-ns rise-time pulse, expected for the R11410 PMTs, we predict an amplitude reduction of 47% and a pulse area loss of 20%.

6.4.3 Assembly and Integration with TPC

The 247/241 PMTs per top/bottom array will be assembled onto titanium support frames. The PMTs will be held in position using Kovar rings fabricated by Hamamatsu from the same material used for PMT body production. Three PTFE columns will then be used to hold the collar to the PMT mounting plates. This mounting system is specified to hold the PMTs in place in the Ti mounting plate both when the plate is in the vertical and horizontal orientations (e.g., during assembly and transport). The arrays are shown in Figure 6.4.3.1, and details of the mounting of the PMTs to the arrays are shown in Figure 6.4.3.2.

The support frames for the PMTs consist of a Ti flat plate with a supporting truss-work. The loads on this structure are substantial, particularly in the case of the lower array. For the submerged PMTs, the buoyancy force on the lower array far exceeds the gravitational force. The net upward load in the lower array is approximately 8 N per PMT, and collectively the total load for the array is approximately 2200 N. Many configurations of the support frame were considered and simulated using finite element analysis. Starting with a bare plate (no truss-work), a single 6-7-mm thick Ti plate deflected upward approximately 19 mm. Other options include successively thicker plates, double plates, curved plates, honeycomb reinforcement, and truss reinforcement. The truss reinforcement had the best overall performance when trying to limit deflection, minimize mass (and therefore background radiation), and provide a relatively open volume for scintillation light in the bottom skin to find its way to skin veto PMTs. The baseline lower PMT support frame is expected to deflect approximately 1 mm upward in operation. The upper PMT support frame will have a similar design, but since the net force is dominated by the weight (the top PMTs reside in gas phase Xe), the expected deflection is approximately 0.3 mm downward in operation.

The Ti surfaces surrounding the front faces of the PMTs, in both the top and bottom arrays, will be covered by PTFE pieces designed to increase the recycling of photons, and so increase photon detection in the main chamber, as discussed in Section 6.5. The pieces are designed to provide >95% coverage of the Ti structural elements, while accommodating the differential thermal contraction coefficients of the PTFE and the Ti mount.

The lower LXe region, below the bottom PMTs and mounting frame, forms part of the Xe skin veto in which the goal is to maintain >95% detection efficiency for ER events above 100 keV. The rear of the bottom PMTs, which project into this volume, are also sleeved in PTFE in order to increase photon

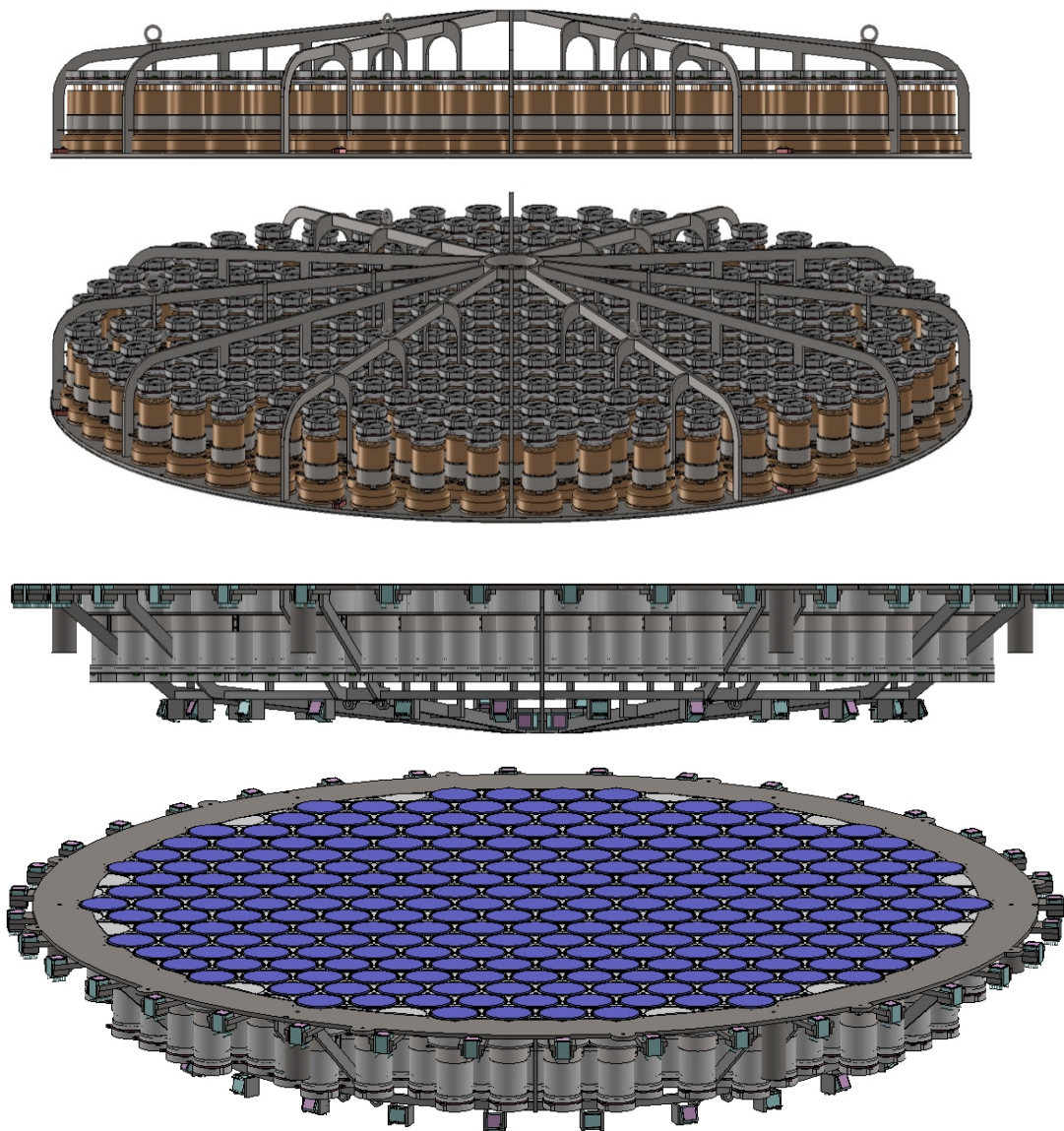


Figure 6.4.3.1. Top (upper two figures) and bottom (lower two figures) arrays of 247 and 241 PMTs. Ti mounting plates and trusses also shown. Details of PTFE reflector system and PMT mounts are shown in Figure 6.4.3.2.

recycling in the LXe below the array — this includes both a PTFE cylinder for the PMT body, and end-caps to cover the PMT bases. The PTFE base covers also prevent stray light leaking into the PMT envelope, and avoid any pin short-circuits.

The underside of the PMT mounting structure and braces will also be covered in PTFE reflectors where required, to increase the overall photon detection efficiency in the skin region.

The PTFE components will be fabricated from material that has been prescreened to achieve the intrinsic activity budget with respect to both gamma and neutron emission, as discussed in Section 6.2 and Chapter 12. During machining of the components and the assembly of the top and bottom PMT arrays, the PTFE components will be maintained in purge boxes to reduce the plating of alpha emitters associated with airborne Rn, and ensure that the additional (α ,n) neutron generation is significantly below the intrinsic neutron emission goals.

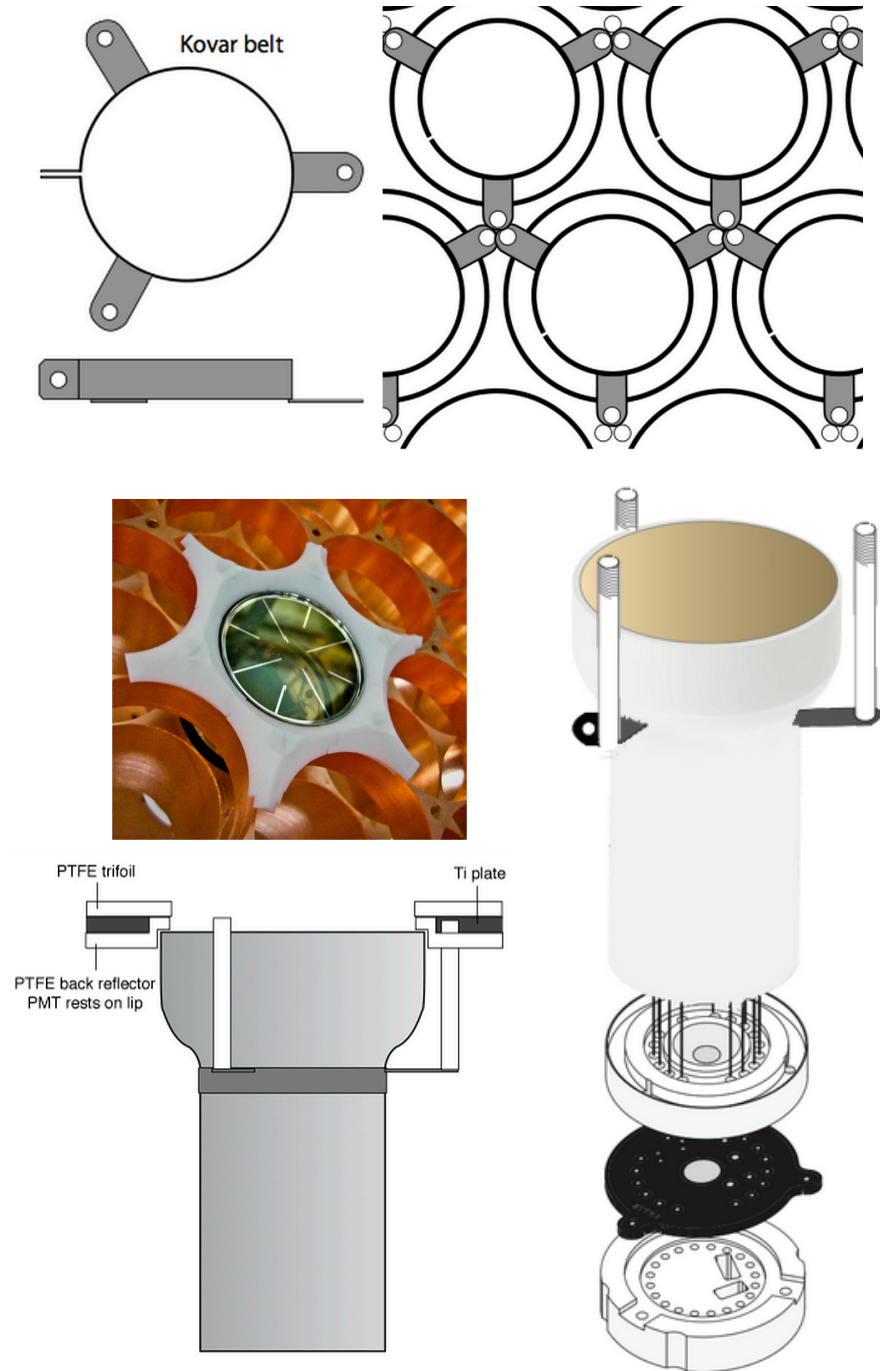


Figure 6.4.3.2. Top: Arrangement of PMT holders and Kovar mounting belt in hexagonal region of PMT array. Photo: Example of front-facing trifoil PTFE reflector used in LUX and baseline design for LZ. Lower left: PTFE reflector arrangement on either side of Ti mounting plate used on bottom array. Top array uses only trifoil front reflectors. Lower right: Assembly of the R11410-20 tube with PTFE sleeve (only used in bottom array) and PTFE end caps (used in both arrays). The latter prevent strain on the PMT stem, protect against electrical shorts in the base, and help relieve strain on the cables. The dark structure represents the Cirlex voltage-divider base.

Calibration LEDs, driven by signals sent down cables that are fed from pulsers in the room-temperature electronics racks, will be mounted in some locations on the face of each array to shine on the PMTs

opposite. The LZ calibration system is closely modeled on the system developed for LUX, which was shown to satisfactorily meet all performance requirements.

6.5 Optimization of Light Collection

6.5.1 Overview of Design and Optical Performance of the TPC

The S1 energy threshold for NR detection in LZ is determined by several factors: (1) the primary scintillation yield of LXe, which is particle-, energy-, and field-dependent; (2) the VUV reflectivity of all PTFE surfaces; (3) the photon absorption length in the liquid, which is determined to be >10 m from operational data in LUX; (4) the geometric transparency and reflectivity of the grids, especially those in the liquid; and (5) the optical performance of the PMTs. The magnitude of S1 also has a strong impact on discrimination, and maximizing the sensitivity of this response channel is an experimental priority. Based on optical simulations and expected PMT performance, we predict a volume-averaged photon detection efficiency $\alpha_1 \approx 7.5\%$ for S1 light in LZ, which will allow us to reach the target threshold and discrimination efficiencies (see Chapter 3).

The S2 channel can easily provide as much gain as necessary, but the layout of the upper PMT array is important to achieve a position resolution <10 mm (rms) at threshold — especially for interactions near the edge of the TPC such as those arising from any contaminants plated out on the field cage walls. The layout of this region has been optimized for this purpose, and the result of these studies is presented in Section 6.5.3 and in Table 6.5.1.1. The adopted baseline is a bottom array of 241 units with close-packed hexagonal layout (third entry in Table 6.5.1.1), and a top array with a hybrid hexagonal/circular arrangement containing 247 tubes (last entry in Table 6.5.1.1). The photocathode coverage represents $\approx 40\%$ of the TPC cross section for each array.

6.5.2 TPC Optical Performance as a Function of Main Parameters

A full optical Monte Carlo based on Geant4 has been used to obtain the baseline photon detection efficiency for S1 light, α_1 , defined as the number of photoelectrons per initial photon generated at the event site. This is discussed in Chapter 3, and summarized in Section 3.4.3. We have adopted a baseline α_1 of 7.5%, along with a range that varies from 5% to 10% or more that reflects a conservatively broad assessment of the possible range of optical properties of the detector materials. Here we describe results from a streamlined Monte Carlo code that complements the full Geant4-based simulation and was used to scan the leading parameters that determine optical performance: the number of PMTs, the reflectivity of the PTFE-LXe interface, absorption length in the liquid, and both the mechanical transparency and reflectivity of the electrode grid wires. The light-collection values from both Monte Carlos agree in most cases to between ~ 5 – 20% . In Figure 6.5.2.1, we first show a map of α_1 as a function of event location for

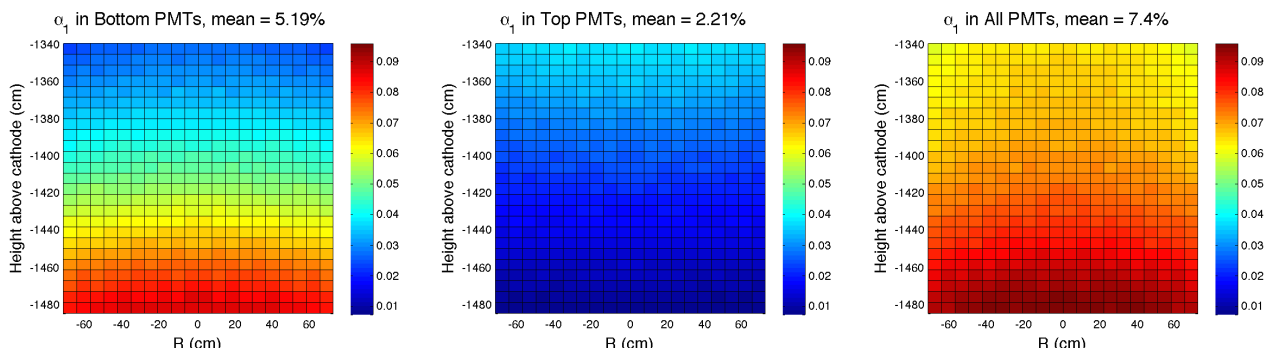
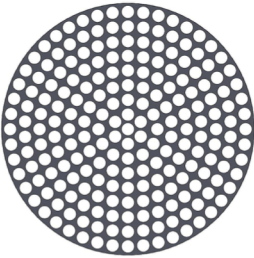
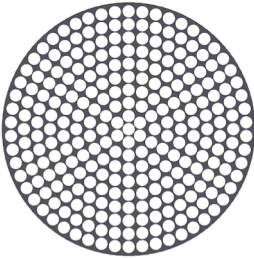
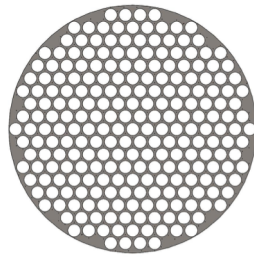
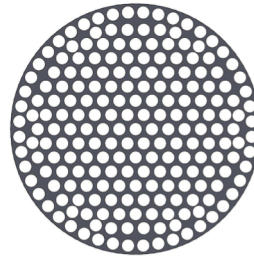
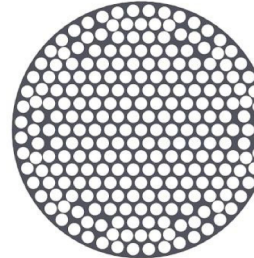


Figure 6.5.2.1. The photon-detection efficiency α_1 as a function of event location in the fully active part of the TPC between the cathode and gate grids, with the baseline values of all optical parameters. The right panel shows the full S1 signal in all PMTs, while in the left and middle panels show those fractions of the signal measured in the top and bottom arrays, respectively.

Table 6.5.1.1. Summary of light collection and position reconstruction performance for candidate top array layouts. The lower half of the table presents spatial resolution *rms* values away from the detector edge with nominal optical parameters; L28 quantifies the fractional leakage of wall events reconstructed more than 28 mm into the TPC.

										
Number	217	271	241	211	247					
Configuration	Circular 1	Circular 2	Hexagonal dilated	Hybrid 1	Hybrid 2					
Spacing	91.0 mm shell radius	80.90 mm shell radius	92.38 mm (all)	83.51 mm (closest)	80.11 mm (closest)					
Notes		Not viable mechanically		1 row circular	2 rows circular, adjusted					
PhC coverage	37.3%	47.1%	43.7%	36.1%	43.1%					
S1 PDE¹	7.8%	8.2%	8.1%	7.7%	8.0%					
S2 pulse: 3,000 emitted photons (270 pe in top array)										
PMT-anode	<i>rms, mm</i>	L28	<i>rms, mm</i>	L28	<i>rms, mm</i>	L28	<i>rms, mm</i>	L28	<i>rms, mm</i>	L28
30 mm	5.3	0.001%	–	–	4.5	2.0%	5.2	0.008%	4.6	0.0001%
50 mm	6.2	0.045%	–	–	5.6	2.6%	6.4	0.075%	5.7	0.028%
S2 pulse: 1,000 emitted photons (90 pe in top array)										
PMT-anode	<i>rms, mm</i>	L28	<i>rms, mm</i>	L28	<i>rms, mm</i>	L28	<i>rms, mm</i>	L28	<i>rms, mm</i>	L28
30 mm	9.3	1.3%	–	–	7.8	8.5%	9.3	1.1%	8.1	0.2%
50 mm	11.0	5.5%	–	–	9.9	13.2%	11.3	4.7%	10.0	2.0%

¹From streamlined MC, with the baseline optical parameters discussed in the text, and averaged over events at $r=0$, for which the yield is $\sim 7\%$ higher than a full volume average.

the baseline parameters (described also in Chapter 3): 25% QE in the PMTs, 95% fully diffusive reflectivity for PTFE in liquid, 20% reflectivity for all grids, 75% reflectivity for PTFE in the gas, and 100 m absorption length in the LXe, as well as the baseline number of PMTs and geometric grid transparencies. The value of α_1 for these parameters in this Monte Carlo is quite close to our adopted 7.5% baseline value. The set of pessimistic and optimistic optical parameters scanned over is indicated in the figures that follow. A key feature evident in Figure 6.5.2.1 is the effect of total internal reflection at the liquid surface, and the optical mismatch between Xe gas and the quartz windows of the PMTs. Photon collection is higher in the bottom array (the index of refraction of LXe and quartz are fairly well matched) than the top array, except just below the liquid surface. Another notable feature is that the average S1 photon path length is ~ 6 m, and the average number of scatters on surfaces that could result in absorption is ~ 5 : To a large extent, the detector is a “mirrored box” in which the value of light collection is the result of a competition between a photon being detected at a photocathode, and absorption that occurs with low probability but a high number of chances as the photon scatters around the detector.

With fixed PMT count and grid opacity, Figure 6.5.2.2 shows some of the main results of the parameter

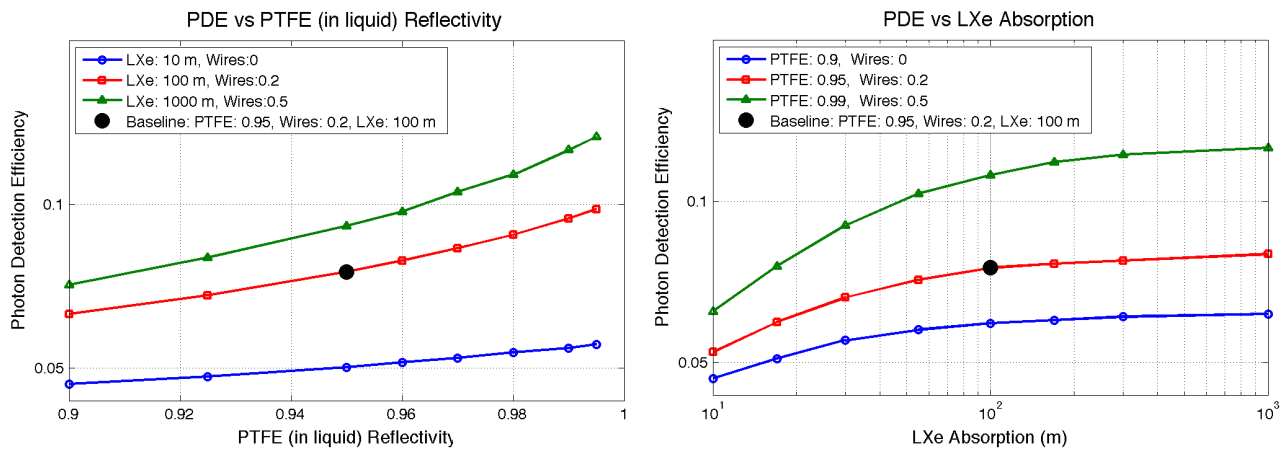


Figure 6.5.2.2. Varying the main optical TPC parameters affects the photon-detection efficiency, α_1 , of the LZ TPC. Left: Dependence of the S1 photon-detection efficiency on PTFE-LXe reflectivity for three scenarios of photon-absorption length and SS grid reflectivity given in the legend. Right: Varying the photon-absorption length in LXe.

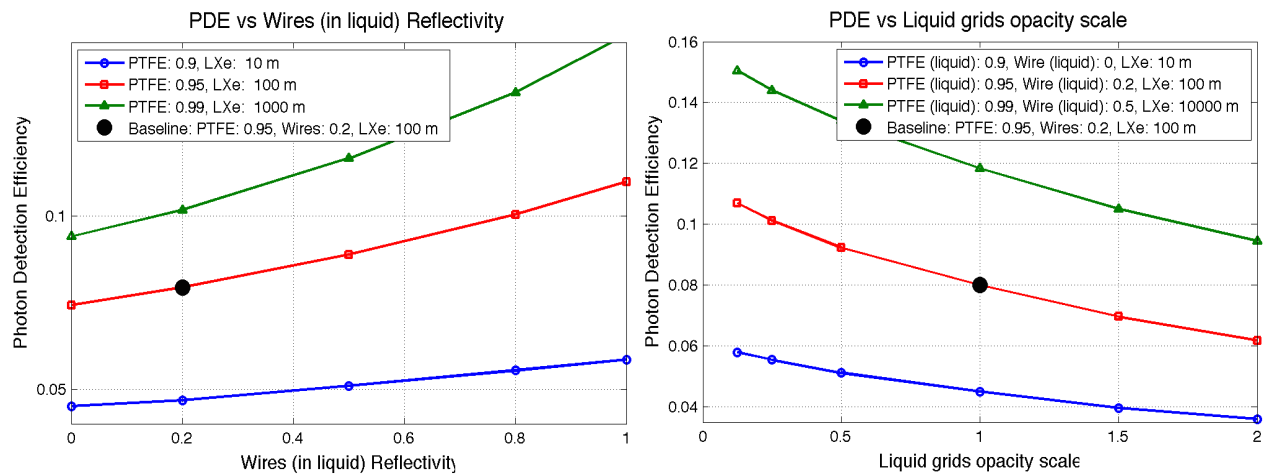


Figure 6.5.2.3. The effect on photon-detection efficiency, α_1 , from varying parameters of the grids. In the left panel, the reflectivity of SS grids is varied, while in the right panel, the opacities (i.e., wire diameter/wire spacing) of all of the grids under the liquid surface are varied together relative to the baseline values (listed in Table 6.1.1), and where transparency = 1 – opacity.

scan. In the left panel, we vary the reflectivity of PTFE in the liquid while holding the other parameters fixed at three plausible sets of values. A range of measurements and modeling of light collection in previous detectors strongly indicate that the PTFE will be diffusively reflective over no less than the range of values shown. The net effect of varying the PTFE alone is as much as ~50%, while the range from varying all parameters is more than a factor of 3 in the most extreme cases. In the right panel, we vary the photon absorption length (l_{abs}) over the range of 10 m to 1 km. Values below ~30 m have significantly reduced light collection. We believe such strong absorption is unlikely based on the VUV absorption cross sections of dominant contaminants such as O₂ and H₂O and their required concentrations to obtain the mean electron lifetimes specified for LZ.

The baseline design of LZ has grids that are relatively opaque in order to reduce electric fields on the wire surfaces. The grids thus have an important effect on light collection, which is explored in Figure 6.5.2.3. The left panel considers a variation in the grid reflectivity, which, if possible, would be achieved by changing the grid material or coating. The limited literature on reflectivity for metals at 178 nm indicates that very high values are unlikely. However, the ongoing HV tests of grids (Section 6.10) may show that more transparent grids are possible. This is explored in the right panel of Figure 6.5.2.3, where all the grids under the liquid surface (bottom shield, cathode, and gate) have their opacity scaled together over a plausible range of values. A 30% improvement or a further 20% loss from the grid opacity alone is possible. A separate scan of the opacity of the grids in the gas (anode and top shield) shows a much weaker ($\pm \sim 10\%$) effect. This is fortunate because, as discussed later, achieving uniform S2 signal pushes the anode grid to be more opaque than any other grid in the detector.

In general, when varied over plausible ranges, PTFE reflectivity, grid reflectivity, and liquid absorption

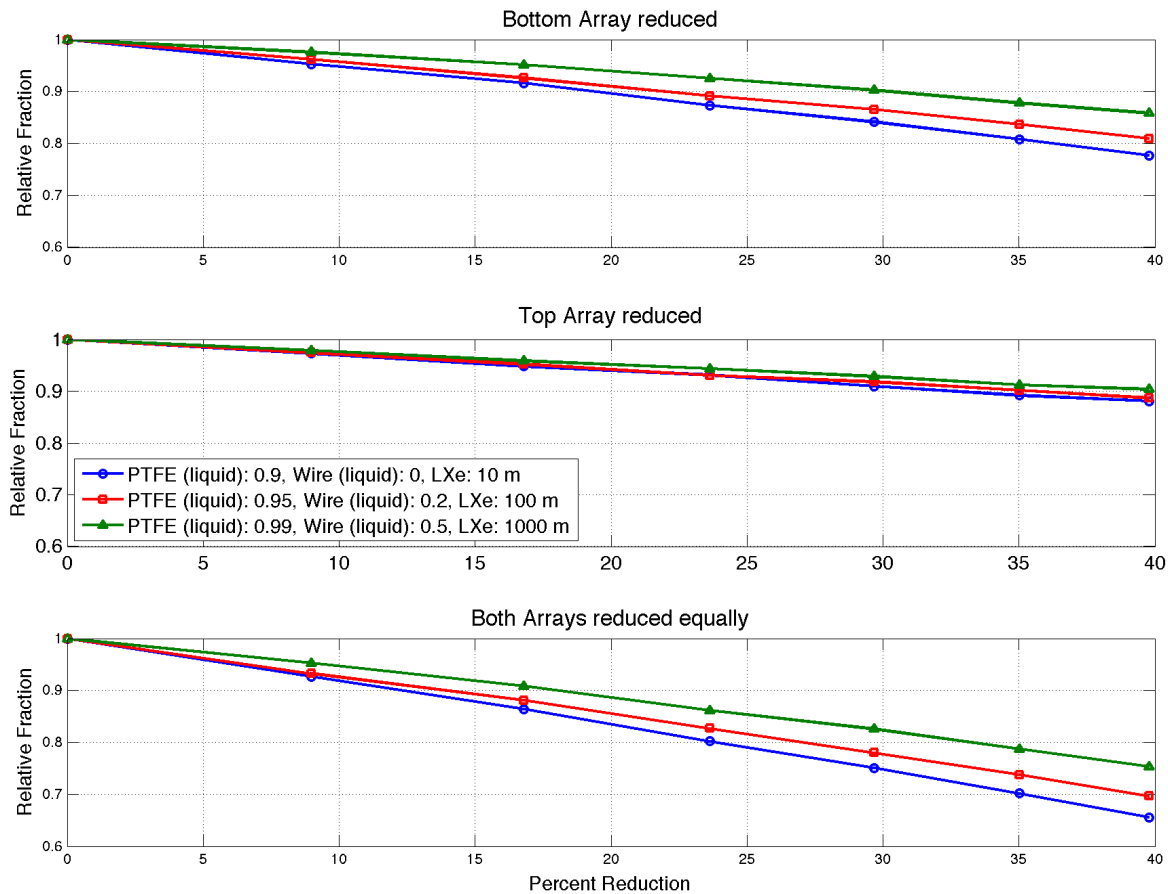


Figure 6.5.2.4. Effect of reducing the number of PMTs in both arrays on the relative photon-detection efficiency for S1 light for the three scenarios indicated in the legend.

length have roughly comparable effects. Somewhat modest gains (or losses) can be achieved by maximizing (or doing less well in) any one of these parameters, while the combined effect of improving (or doing worse in) all three could result in perhaps doubling (or near halving) of the overall light collection. We believe the baseline parameters we have adopted are somewhat conservative, and hope to be able to select materials so that we achieve α_1 above 7.5%.

Concerning the PMT count, the best performance for S1 light is naturally obtained with the maximum packing fraction on the bottom array, which is 241 units. The top array configuration is driven by other considerations, which are described in detail later. The same streamlined simulation was used to assess how the light yield is worsened as the number of PMTs in either or both arrays is reduced. This is shown in Figure 6.5.2.4. As expected, descoping the bottom array is more damaging than descoping the top if the remaining optical parameters are not all extremely good: With more extinction in the chamber, the refractive index mismatches at the liquid/gas and gas/quartz interfaces lower the fraction of S1 light collected by the top array. The bottom array avoids both effects since quartz and LXe are well matched optically.

6.5.3 Optimizing the TPC Array Configuration

The design drivers for the two PMT arrays that read out the TPC are not identical, and this motivates the different layouts adopted. The bottom array provides most of the detection efficiency for S1 photons ($\approx 70\%$), which determines the NR energy threshold and discrimination efficiency. This is mostly due to the total internal reflection at the liquid surface above a critical angle of 36° and the good match in the VUV of refractive indices between the quartz in the PMT windows and LXe. Maximum photocathode coverage of the TPC cross section is therefore the main requirement. In contrast,

the principal function of the top array is to reconstruct S2 events and provide spatial resolution in the horizontal plane. Especially critical is the accuracy of reconstructing the x-y position of “wall events” that result from interactions near the vertical cylindrical surface of the PTFE that defines the TPC. The placement of the outer few PMT rows is critical: Misreconstruction of peripheral interactions further into the TPC volume can lead to a significant reduction in fiducial mass.

The optimization of the bottom array was straightforward, involving mechanical considerations and Monte Carlo simulation of S1 light-collection efficiency. A close-packed hexagonal layout of 241 tubes fully contained within the TPC diameter (Figure 6.5.3.1, left) was selected as the baseline. The axis-to-axis separation of the PMTs is 91 mm, for a cut-out diameter of 80 mm. Reducing PMT numbers in the bottom array lowers the overall S1 photon-detection efficiency, especially if the photon extinction provided by surface and bulk absorption is more severe than anticipated.

The top array layout is driven to a significant extent by the need to correctly reconstruct low-energy background events from the TPC walls. In particular, radon progeny plated out on the PTFE can lead to a significant population of events, including NRs from α decay (where the α -particle goes into the wall) and low-energy ERs, which can also be dangerous due to loss of charge at the wall. In contrast to the bottom array design, which is fully contained within the TPC diameter, the top array must overhang the

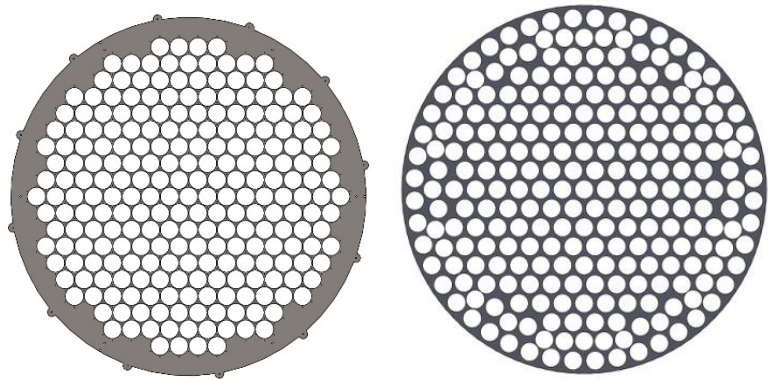


Figure 6.5.3.1. Left: Bottom array configuration with 241 tubes in close-packed hexagonal configuration. Right: Top array layout with 247 units, a hybrid configuration consisting of a hexagonal matrix with two (nearly) circular outer rows.

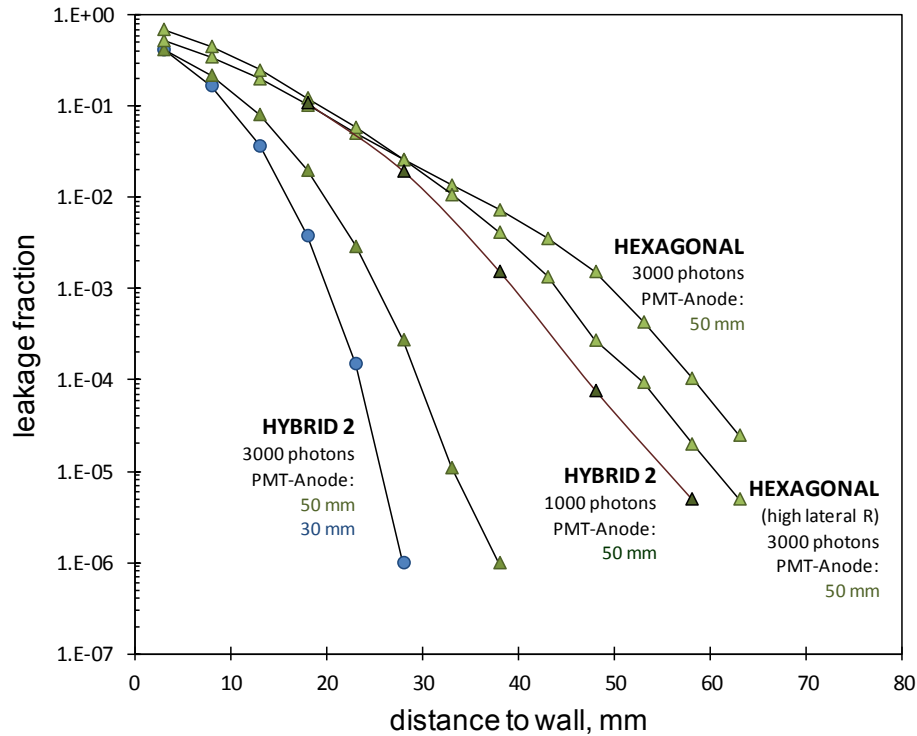


Figure 6.5.3.2. How the leakage fraction varies with the array configuration for the best and poorest layouts studied, as well as lateral reflectivity in the gas phase (60% for the high-reflectivity scenario and 0% for the others), and the distance between the PMT windows and the anode electrode. The fiducial volume with 5.6-tonne mass starts 39 mm from the wall.

edge of the TPC or all the reconstruction bias will point inward. Ideally, at least a full row of tubes would be located beyond the inner radius of the chamber. This is not possible due to the proximity of the inner cryostat vessel, and instead we locate the outermost circle of tubes at the largest-possible radius, which aligns the PMT centers above the TPC wall.

Five layouts were considered; these are depicted in Table 6.5.1.1, which also summarizes key parameters and the results from the optimization exercise. We include two circular arrays of 217 and 271 units (the latter was subsequently found not to be mechanically viable), a hexagonal array of 241 units slightly dilated with respect to the bottom array, and two circular/hexagonal hybrid arrays containing 211 and 247 PMTs.

The methodology employed to determine which array configuration is best suited to minimize wall leakage involved extensive optical Monte Carlo coupled to the Mercury vertex reconstruction algorithm used in ZEPLIN-III and LUX Run 3 [13]. This provided a realistic assessment of the position resolution of the chamber for very small S2 signals and, in particular, the fraction of peripheral events that is misreconstructed into the TPC volume. This “leakage” fraction was the main design criterion used to select the best array configuration.

Two other design parameters influence the peripheral position resolution and were therefore included in this study. These are the distance between the anode grid and the PMT windows, and the reflectivity of the lateral wall in the gas. Regarding the latter issue, a low-reflectance material is desirable so as not to distort the response of the outer PMTs. Titanium has $\approx 16\%$ reflectance at 178 nm, but its oxides can be significantly more reflective in the VUV [14]. We studied a high-reflectance scenario (PTFE) as well as values in the range of 0–30% that could be achieved by anodizing titanium or employing a thin layer of a polyimide such as Kapton, which is essentially black in the VUV [15].

For each array configuration, in an initial study the Mercury algorithm was trained to obtain axially symmetric light response functions (LRFs) for each PMT using simulated S2 light. Then, very small S2 signals were simulated and randomly distributed in (x,y) or at the TPC walls with 1,000 photons (~ 90 phe collected in the top array, coming from an initial ~ 4 emitted electrons) and 3,000 photons (270 phe in the top array, and ~ 12 electrons). The position was obtained by fitting to all channels simultaneously. The reconstruction *rms* for events near the middle of the detector (more than 130 mm from the wall), and the leakage fraction, are summarized in Table 6.5.1.1. The latter is defined here as the fraction of events located at the wall, which are reconstructed to more than 28 mm from the wall. The hexagonal array performs noticeably worse due to the poor coverage in some positions. The hybrid with 247 PMTs (Figure 6.5.3.1, right) is the best, and this is our baseline. With the exception of the hexagonal array, the other layouts do not perform significantly worse from this point of view. We also considered the distances from anode to PMT array, and the reflectivity of the wall in the gas (at and above where the S2 light is generated). The best performance is obtained with the anode as close as possible to the PMTs.

The reflectance of the wall in the gas region has a mixed effect, sometimes improving and sometimes decreasing performance, an issue that is under further study. Our baseline design is based on a distance of 48 mm between anode and top PMTs, of which 38 mm are between the anode and top shield grid, and 10 mm between this grid and the top PMTs.

Finally, in Figure 6.5.3.2 we show the results from an improved and higher-statistics study of the leakage past the 39-mm distance of the nominal 5.6-tonne fiducial volume. This was done for the baseline hybrid array, and the 241 PMT hexagonal array. The strong signal size dependence of the leakage is apparent, as well as the improvement of the hybrid array over the hexagonal array. The leakage into the fiducial volume is small except at the lowest-possible values of S2.

6.6 Optimization of the Electroluminescent (S2) Signal Production

The extraction/electroluminescence region of the TPC is located at the top of the field cage, with the gate and anode electrodes (nominally 10 mm apart) straddling the liquid surface. The liquid level is controlled by a weir system at the edge of the TPC, which is detailed below. This region generates a light signal proportional to the number of electrons drifted away from the interaction site via proportional scintillation in the gas phase, readily providing sensitivity to single electrons emitted from the liquid, as discussed in Chapter 3.

Three main parameters characterize the S2 response: the photon yield, which depends on both the electroluminescence production and the surface extraction probability for electrons; the pulse width, which is proportional to the electron transit time in the gas phase to first order; and the resolution of the S2 signal, which depends on several parameters discussed below. These characteristics depend on operating parameters such as vapor pressure, length of the gas gap, and the voltage applied between the anode and gate electrodes. The S2 performance is also affected by other electrostatic considerations (e.g., maximum fields that can be sustained at the wire surfaces) and mechanical feasibility (e.g., limitations on the manufacture of large wire grids, wire sagging, etc.). In the following sections, we highlight baseline and “maximum” design scenarios, and describe how the S2 response depends on the operating conditions. Key parameters are presented in Table 6.6.1. The size of the S2 signal also depends on the efficiency of light collection. We here assume 9% based on a preliminary Monte Carlo, which uses a crude treatment of the grids, though we anticipate that this value may decrease as the grids are treated more accurately.

Baseline Design

For the smallest S2 signals, generated by 1 to a few ionization electrons, the main S2 requirements are: (1) definition of the single-electron response with a high S/N ratio, to allow absolute calibration of the ionization channel, and to enable physics searches down to S2 signals as small as a few electrons; and (2) sufficiently large S2 signal for accurate reconstruction of the x-y location of peripheral interactions, such

Table 6.6.1. Summary of electroluminescence region design parameters.

	Baseline	Maximum	
Gate, kV	-4	-7	Grid: 5 mm / 100 μm^*
Anode, kV	+4	+7	Grid: Woven wire mesh
Top grid, kV	-1.0	0	Grid: 5 mm / 50 μm^*
Extraction field, kV/cm	10.6	11.1	In gas
Distance from liquid surface to anode, mm	5	10	
S2 yield			
Photons/e-	550	1,200	(Parallel field approx.)
phe/e-	50	110	(PDE=9% top array)
Fields (kV/cm)			
On surface of gate wires	75	79	In liquid, with cathode at 100 kV
Above anode	1.3	1.8	In gas
On surface of top shield wires	25	10	In gas

* Wire pitch / diameter

as those arising from contamination on the TPC walls. This motivates a photon yield of at least ~ 50 photoelectrons detected in the top array per emitted electron (cf. ≈ 31 in the first run of ZEPLIN-III [16] and ≈ 25 in LUX Run 3 for both arrays [17]). More details on how the S2 pulse size affects the reconstruction of wall events are given in Section 6.5.3.

Considering an S2 photon-detection efficiency of $\sim 9\%$ for the top array, predicted by simulation, the

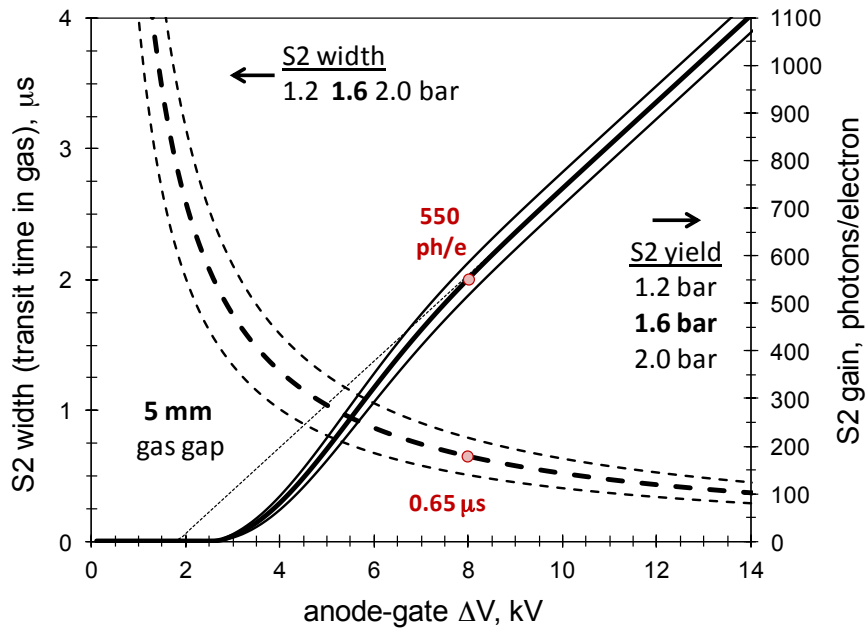


Figure 6.6.1. Dependence of the S2 photon yield and S2 pulse width (for emitted electrons, i.e., ignoring longitudinal diffusion in the liquid) on the voltage between anode and gate electrodes. At the nominal $\Delta V=8$ kV, the photon yield [18], including the electron emission probability [19] and the electron transit time in the gas phase (S2 pulse width) [20] (for operating pressures around the 1.6 bar nominal and a gas gap of 5 mm) are shown.

above photoelectron yield implies 550 photons generated per emitted electron. For a gate-anode distance of 10 mm with the liquid level halfway between them — our nominal design — this is achieved with a gate-anode voltage of 8 kV at the operating pressure of 1.6 bar, as shown in Figure 6.6.1. We plan to apply +4 kV to the anode and −4 kV to the gate, leaving the liquid surface near −1.3 kV.

The required yield can be achieved with other combinations of anode-gate separation (L), length of the gas gap (L_g), overall applied gate-anode voltage (ΔV), and vapor pressure (P). All of these parameters are intimately connected to S2 light production: Both the electroluminescence yield and the electron drift velocity in the gas are determined by the reduced electric field in that region, E/P ; in addition to the applied voltages, the electric field depends on both L and L_g . Therefore, these parameters must be studied together and their optimization is subtle. We describe below some of the main arguments that motivated our baseline design for the electroluminescence region, with reference to Figures 6.6.1 and 6.6.2. We postpone the discussion of how the actual electrodes are implemented until the end of this section, focusing here on mean yield values only.

The electron emission probability at the liquid surface decreases rapidly when the field in the gas drops below 10 kV/cm [19]. In Figure 6.6.1, the S2 yield assuming full extraction efficiency is represented by the dotted line, while the continuous lines include the field-dependent extraction probability. For our nominal parameters, that probability is close to unity. Increasing the S2 yield by increasing the length of the gas phase may appear desirable, but it may lead to low extraction if nominal voltages fail to be achieved, or if they need to be reduced to preserve linearity for larger signals.

Longer electron transit times in the gas also hide the effect of electron diffusion in the liquid, which encodes interaction-depth information on the S2 pulse shape. This information allows some coarse fiducialization, which is important for the S2-only analysis. On the other hand, too short an S2 signal may be adverse for robust pulse identification, causing confusion with S1 pulses and other topologies; we wish to maintain this parameter to be $\geq 0.2 \mu\text{s}$. Very short gas gaps are also problematic for practical reasons: the need to level the detector with extremely high precision, to cope with the inevitable sagging and electrostatic deformation of the anode and gate grids, and to achieve homogeneous fields above the gate, which has a wire pitch of order millimeters. A nominal anode-gate distance of 10 mm with a gas thickness of 5 mm is a reasonable compromise, leading to a transit time of $\sim 0.65 \mu\text{s}$ for $\Delta V=8 \text{ kV}$.

High-yield Design Maximum

Our understanding of the reconstruction of “wall events” is still evolving, informed by LUX data and optical simulations such as those described in Section 6.5.3. Although the S2 gain cannot be arbitrarily

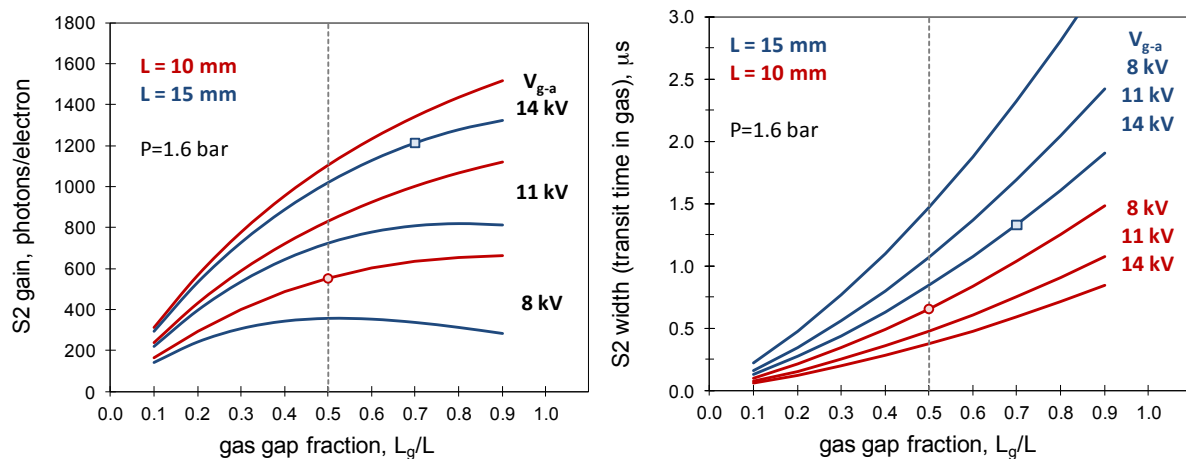


Figure 6.6.2. Variation of S2 gain (left) and S2 width with gas gap for anode-gate distance of 10 mm and 15 mm, and for several gate-anode voltages. The S2 gain includes electroluminescence photon yield and emission probability. The S2 width applies only to emitted electrons since it ignores diffusion in the liquid. Baseline and design maximum scenarios are indicated by the round and square markers, respectively.

large due to the limited dynamic range of the optical readout, we will continue to consider in parallel a more aggressive S2 design with a larger gas gap of 10 mm (for an electrode separation of 15 mm) and higher applied voltages, $\Delta V=14$ kV. These changes require only modest hardware modifications. Although this design involves higher fields near the electrodes and may compromise the diffusion information due to longer transit times in the gas, it is also less aggressive on mechanical requirements involving detector leveling and grid sagging — besides doubling the S2 gain. The mean S2 yield for this scenario is $\sim 1,200$ photons per emitted electron (110 phe/e) and the mean transit time in the gas is 1.3 μs . This design involves application of higher voltages to electrodes in the gas phase, which may create regions with electric field above the electroluminescence threshold of ~ 2 kV/cm; we avoid this in the region between the anode and the top grid (which protects the top PMT array) by bringing that electrode to ground in this case. Another critical parameter is the maximum field at the surface of the anode wires, which is addressed below.

Electrode Configuration and S2 Energy Resolution

In addition to appropriate S2 gain and pulse width, we must ensure that the S2 resolution is as good as it can be, primarily so that that ER/NR discrimination at low energies is not compromised by the adopted S2 design and, more generally, that the S2 channel has high resolution, especially at higher energies. This is intimately related to the quality of our calibration (e.g., ^{85}Kr signals with $\sim 1,000$ ionization electrons) and the characterization of detector backgrounds (e.g., radioactivity gamma rays with up to $\sim 10^5$ electrons). Our goal is for the ER bandwidth (a key parameter for ER/NR discrimination) to be dominated by recombination fluctuations in the liquid — which affect the number of electrons extracted from particle tracks — and S1 light-collection and photoelectron statistics, since these parameters cannot be improved easily. Therefore, fluctuations related to S2 photon production and measurement must remain small, at the level of a few percent. This motivated the detailed study of electroluminescence and electrode grid configuration, which is summarized below. Other factors contributing to the S2 resolution are the uniformity of response in the horizontal plane over the scale of the whole TPC diameter (e.g., wire sagging and electrostatic deflection), though those in principle can be calibrated and hence removed.

Aside from diffusion (in both gas and liquid phases), drifting electrons follow electric field lines and therefore their length and the field strength close to the wires must be carefully controlled to avoid substantial dispersion or even the possibility of significant charge multiplication (the first Townsend coefficient for cold Xe vapor at our operating pressure reaches ~ 1 e/mm at 35 kV/cm [20,21]). Two additional concerns, which are intimately related, are the HV resilience of the electrodes and their VUV reflectivity, which depend strongly on the wire surface quality and material or coating; we are investigating these issues through the dedicated R&D activities described in Section 6.10.

The optimization of the anode geometry involves a compromise between optical, electrostatic, mechanical, and electroluminescence properties. The latter were assessed through full electron transport modeling, in particular examining the S2 photon production statistics from single electron drifts in the gas phase of the various candidate geometries. A combination of software was used for this purpose. Garfield++ is a Monte Carlo simulator for electrons in drift chambers [22]. Electrons are microscopically tracked as they drift, and the locations of any excitations or ionizations are recorded. An excitation is assumed to produce one photon, and ionizations give extra electrons, which are also tracked. It can calculate electric field maps for simple configurations where an analytical solution exists. This limits it to 2-D geometries consisting of planes and wires. To calculate the electron transport properties of the gas, Garfield++ is interfaced to Magboltz [21], which relies on elastic and inelastic cross sections for gases to calculate the relevant transport parameters (drift, diffusion, and gain). To simulate electric fields from 3-D geometries, field maps were created using the Elmer solver [23] and the meshing tool Gmsh [24]. The field map was then read by Garfield++ for tracking. In Figure 6.6.3, we show equi-field contours for unit cells of three of the wire-grid geometries considered: a simple crossed-wire arrangement, which allows low mechanical deformation relative to a parallel wire plane; a fine-woven mesh such as that used in

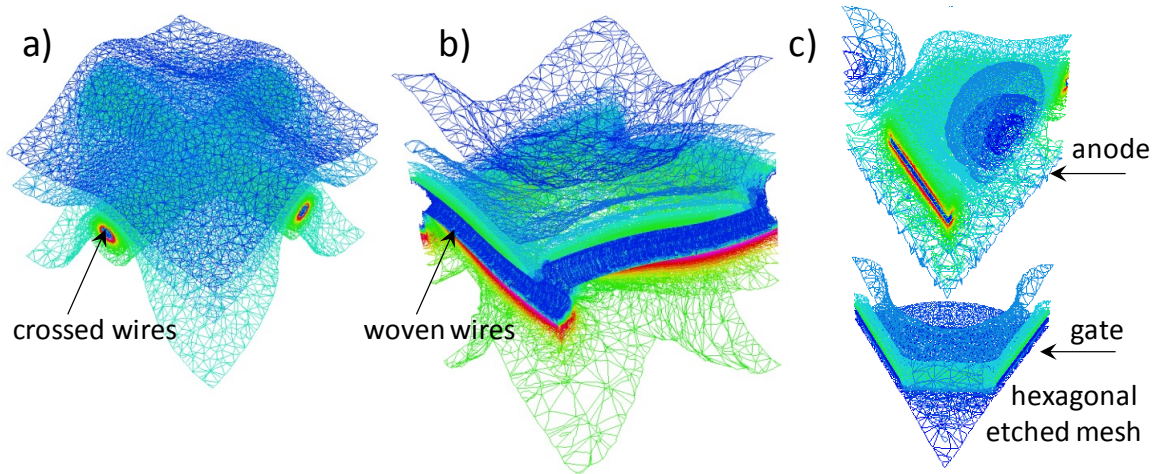


Figure 6.6.3. Electrostatic models for several anode configurations calculated using Elmer [23] and meshed with Gmsh [24]. The crossed-wire mesh (a) and the LUX-style woven mesh (b) are both candidate configurations for the LZ anode; in (c) we show the unit cell for the XENON100-style hexagonal etched meshes (gate also shown).

LUX; and an etched hexagonal grid-set similar to that used in XENON100 [25]. The latter geometry required implementation of the gate electrode to simulate electron focusing; these hexagons were created with three different wire-rounding values of 0%, 10%, and 40%.

In our simulation study, we confirmed that the woven mesh used in LUX produces very small dispersions of photon production (typically <1%) for a range of operating conditions, never far from the values obtained for the parallel configuration in ZEPLIN-III, where the anode was a solid plate (no top PMT array and no gate grid) [26]. We compare these values with the fluctuations expected from photoelectron statistics for single electron signals, which is of order 15% and, more importantly, with the best S2 resolution achievable at MeV energies by EXO, which is 1–2% [27]. It is therefore desirable to keep photon-production fluctuations to a maximum of ~2% so that this does not compromise the performance of the instrument for background characterization, calibration, and non-WIMP signals.

The fine LUX woven mesh has 30- μm wire diameter and 250- μm pitch and is our baseline for LZ if a suitable manufacturer can be identified that can accommodate the large diameter required. The optical transparency of this mesh is acceptable (80%) and the maximum electric field at the wire surface is modest. The properties for this choice are listed in Table 6.6.2.

Table 6.6.2. Main electroluminescence properties calculated for a LUX-like woven-mesh anode (LZ baseline); a gate-anode voltage difference of 8 kV is assumed, along with a nominal gas gap of 5 mm. The S2 photon yield is calculated as described above and also from the simple parallel-plate approximation and experimental electroluminescence yields from [18], for direct comparison with Figure 6.6.1.

	Value	Notes
Wire diameter	30 μm	
Wire pitch	250 μm	
Optical transparency	79.7%	Normal incidence
Maximum wire field	33 kV/cm	Elmer
Photon yield	583 ph/e	Garfield++
(Parallel plate)	550 ph/e	Parameterized yield
Photon RMS	0.26%	Garfield++

Table 6.6.3. Alternative anode configurations explored through Garfield++ simulations. The table lists, for parallel and crossed-wire configurations: the mean S2 photon yield per electron emitted from random locations below the unit cell (ph/e) and relative width of the photon distribution (percent *rms*), both given to last (statistical) significant digit; the maximum electric field at the wire surface, E^* , in kV/cm; the optical transmission at normal incidence, T . A gate-anode voltage of 7.5 kV was assumed in this case, which is lower than the adopted value of 8 kV; a nominal gas gap of 5 mm is considered in all cases.

Wire pitch →	1 mm				2 mm				3 mm			
	ph/e	<i>rms</i>	E^*	T	ph/e	<i>rms</i>	E^*	T	ph/e	<i>rms</i>	E^*	T
Parallel wires												
50.8 μm	530.5	1.23%	60	94.9%	572	8.9%	105	97.5%	1066	47%	140	98.3%
101.6 μm	529.9	0.63%	36	89.8%	529.1	2.53%	62	94.9%	560	9.7%	82	96.6%
203.2 μm	530.3	0.53%	22	79.7%	527.1	1.23%	36	89.8%	523.2	3.1%	48	93.2%
Crossed wires												
50.8 μm	530.7	0.69%	30	90.6%	527.2	1.91%	56	95.1%	528.8	4.3%	76	96.7
101.6 μm	531.1	0.68%	19	82.4%	528.4	1.36%	51	90.6%	526.3	2.49%	47	93.6
203.2 μm	531.5	0.72%	15	69.1%	528.3	1.41%	21	82.4%	525.2	2.19%	25	87.7

We studied also three other anode configurations that could be suitable for LZ: grids made from parallel wires or from crossed wires, as well as the hexagonal anodes of the type used in XENON100, made from chemically etched SS plate. The latter offers high optical transparency and acceptable photon production dispersion ($\approx 1.2\%$), but it leads to significant fields at the metal surface (~ 100 kV/cm) and the potential for some charge multiplication, which indeed we recorded in some of our simulations.

We focused instead on the parallel- and crossed-wire configurations listed in Table 6.6.3. Clearly, the parallel-wire grid is less attractive from a mechanical point of view, since it lends itself to significant deformation — and it leads to higher fields at the wire surface (up to a factor of 2 relative to the crossed-wire version) and higher S2 dispersion in general. A good alternative to the very fine-woven mesh used in LUX is the crossed-wire grid with 100- μm wire at 2-mm pitch. The remaining configurations are mostly acceptable, except for the 50- μm wire at 3-mm pitch ($rms > 4\%$) and 200- μm wire at 1-mm pitch ($T = 69\%$).

6.7 Design and Optical Performance of the Skin Detector

The design of the TPC located inside the LXe inner vessel requires that a physical buffer region be between them. This region provides necessary mechanical clearance to allow detector assembly, houses detector instrumentation including the PMTs, and, most importantly, is used to limit the maximum electric field gradients by providing a standoff between biased TPC components and the electrically grounded inner vessel. We instrument this buffer region, or “Xe skin,” as part of our anticoincidence strategy to identify backgrounds that scatter within these regions with high efficiency. The Xe skin is divided into two primary functional regions: a cylindrical (side) skin region outside of the main TPC field rings, and a dome skin region underneath the TPC, below the bottom PMT array.

The side and dome skin regions contain a total of more than 2 tonnes of LXe and are viewed by 180 dedicated 1-inch R8520 PMTs. This Xe skin detector performs a similar and complementary function to the outer LS detector. If the skin regions were filled with passive filler material, the efficiency of the background rejection by the veto would be substantially degraded due to the absorption of secondary scatters that would otherwise have been tagged in the outer detector. The goal for the Xe skin detector design is to achieve a clear anticoincidence detection threshold for ER scatters directly from gamma-ray

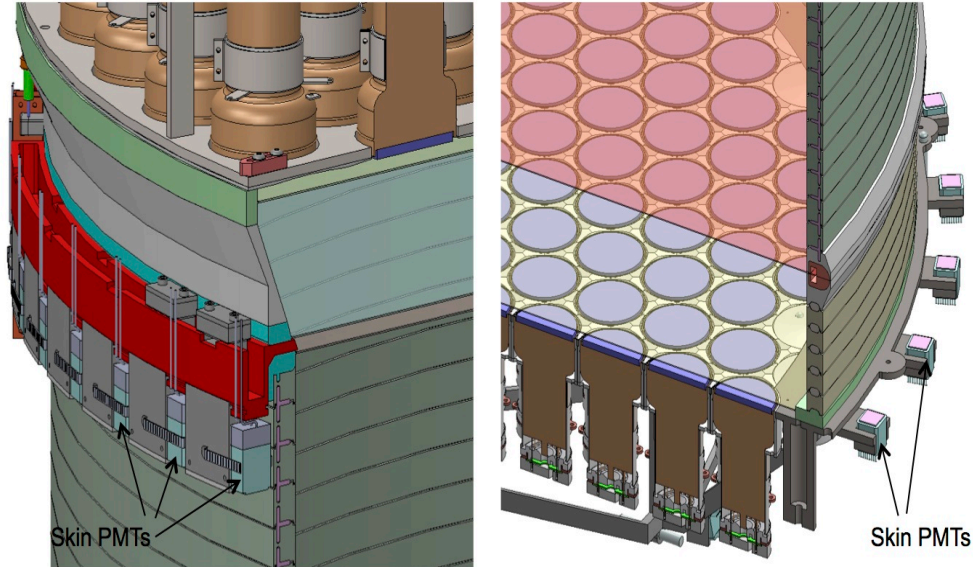


Figure 6.7.1. Arrangement of skin photomultipliers. Left: Side PMTs near top TPC array. Right: Side and dome PMTs below bottom TPC array. Extensive PTFE lining is required to minimize photon extinction in the skin region.

backgrounds, or gamma rays from thermal neutron capture, at a deposited energy of 100 keVee in 95% of the volume of the Xe skin.

It should also be noted that for events that deposit energy in both the main TPC and the LXe skin region, leakage of light from the skin to the TPC can compromise the primary S1/S2 background rejection if the (non-leaking) signal in the skin is below threshold. This is because the leakage light from skin will add to the S1 signal from the TPC and lower the S2/S1 ratio used for particle discrimination. Random coincidences between the two regions can also lead to false vetoing of fiducial interactions. For these reasons, it is important to directly instrument the outer LXe to clearly identify events with a scattering vertex in the outer region and also to minimize light leaks between inner and outer regions with good design of the intermediate wall.

The side skin region will be 4 cm wide near the top of the TPC, increasing to 8 cm in the lower half due to the tapered vessel shape. In the baseline design, this region is instrumented with 60 1-inch R8520 PMTs viewing down located just below the LXe surface, and a further 60 looking up located at the same level as the lower PMT array. The inside surface of the inner cryostat vessel is lined with thin PTFE sheets for improved light collection. The outer surface of the TPC also provides a PTFE reflector.

The dome skin region below the lower PMT array will be instrumented with another 60 1-inch R8520 PMTs. PTFE will be used to cover the components in this region to improve light collection with an overall goal of 95% coverage. The R11410 and R8520 PMTs will have reflective PTFE sleeves to reduce photon absorption on their side and rear walls. The placement of the skin photomultipliers is depicted in Figure 6.7.1.

The skin region uses the 1-inch PMTs, rather than the larger model in the TPC due to mechanical constraints. The Hamamatsu R8520 is specifically designed for LXe operation. It was the primary PMT used, for example, in the XENON10 and XENON100 detectors [12,25]. This is a very compact 1-inch-square PMT with quartz window and bialkali photocathode with a typical QE of 30% at 175 nm. A gain of 10^6 is provided by an 11-stage metal channel dynode chain. These can be operated with passive voltage divider bases with either negative or positive bias.

The design studies for the LXe skin used a detection threshold goal of 100 keVee for at least 95% of the volume of both the side and dome regions. Threshold detection requires a 95% efficiency for observing at

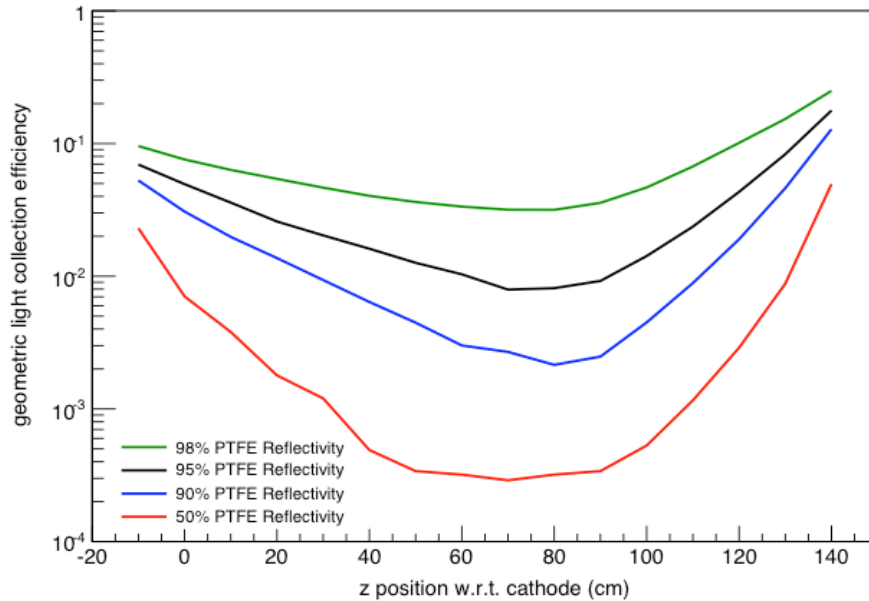


Figure 6.7.2. Effective light-collection efficiency calculated from light simulations, for a vertical profile in the LXe side skin region, using a range of assumptions for the reflectivity of the PTFE lining the region. The position of the interaction is measured relative to the cathode in the TPC. The vertical scale is light-collection efficiency, taking into account absorption in the walls and liquid (but not the QE of the tubes). A 100 keVee event in a high field region yields 2,150 VUV photons. A value of just under 1% LCE (bottom of 95% reflectivity curve) corresponds to a 95% detection efficiency for 3 phe when using 60 top and 60 bottom R8520 PMTs.

least 3 phe coincident (in a 100-ns window) in the R8520s from the primary scintillation light event. The R8520 PMTs are assumed to have typical 30% QE, and the light yields in the LXe are assumed to be suppressed (by as much as 65% from zero field values) by the electric fields between the TPC and the inner vessel wall, which will be present during the operation of the TPC. A PMT coverage of 60 upper + 60 lower 1-inch PMTs was able to achieve this veto threshold performance goal in the dome skin region. As shown in Figure 6.7.2, the lowest efficiency for light collection in the skin region occurs in the region equidistant between the upper and lower PMTs, where it falls by over a factor of 5 compared with the regions closer to the skin PMTs. Given the simulated light collection, the energy threshold target of 100 keV in the side skin can be achieved assuming a conservative value of 95% reflectivity for the walls of the lateral skin region. The effective energy threshold scales close to linearly with the number of PMTs used in this region.

The dome skin region is a less regular shape than the side region, and houses a number of components, including the bottom TPC PMTs, the Ti plate and trusses to support the array, bases, cabling, and LXe fluid plumbing. More conservative assumptions were made in the simulations for the net reflectivity of the surfaces in this space, using only 90% average reflectivity to account for breaks in the PTFE reflectors. In simulations, in order to achieve a 100 keVee identification threshold (with 95% likelihood of ≥ 3 phe detected) for interactions in 95% of the LXe volume (i.e., voiding the requirement for the 5% of LXe skin that is most difficult to collect light from), it is necessary to use 60 x 1-inch PMTs. The baseline design calls for thirty PMTs to be housed in a ring at the periphery of the region, interspersed with the lower PMTs of the LXe skin, but pointing downward, rather than up. The other 30 will be distributed on the truss structure. To maximize the light signals, the rear and sides of the R11410 and R8520 PMTs are sleeved in PTFE (see Figure 6.4.3.2) and their bases covered with a PTFE cap. In addition, the internal fluid piping and cabling trusses and the surface of the inner vessel will be covered with, or made from, that material. Again, in the light propagation models tested, increasing PTFE

coverage to include all components significantly reduces the number of PMTs required to cover this region. Economizing on the number of PMTs comes at the expense of more PTFE reflectors.

6.8 Internal Fluid System

Efficient purification of LXe is a significant challenge, and is especially important given the large size of LZ and the resultant long electron drift lengths and long photon path lengths. Purification is discussed in detail in Chapter 9, and the overall internal flow diagram is shown schematically in Figure 6.8.1. Liquid in the detector is continuously circulated to a purification tower located outside the water tank, where it is evaporated in a two-phase heat exchanger and passed to a gas system. There, it is purified by a commercial heated getter. While the getter is highly efficient in a single pass, continuous purification has proved necessary in most previous such detectors, primarily because of the large amount of PTFE and other plastics (e.g., cables) in the TPC that serve as a long-term source of outgassing. After passing through the getter, the Xe returns to the liquid tower, where it is recondensed in the two-phase heat exchanger, degassed and subcooled, and then passed back to the detector. In addition, separate gas flow through the external purification system purges the spaces above the liquid. The overall flow rate is 500 slpm of gas, or roughly 1 liter/min liquid flow.

While most of the functionality and complexity of the system is external to the Xe detector system and is described in Chapter 9, several important elements of the design are in the Xe detector system and are described here. This “internal circulation system” has several goals: effective circulation of both liquid and gas; establishing and controlling the thermal environment of the detector, including suppressing bubble formation and providing convective mixing to disperse internal radioactive sources; and maintaining a stable and quiet liquid level at the surface of the detector.

The liquid circulation paths are designed to efficiently sweep all of the liquid regions. Separate tubing sets are used to direct individually controlled flows into the bottom of the TPC, the lower part of skin, and the two liquid-filled conduits (HV and bottom cabling/fluid). The plumbing paths in the central region are shown in Figure 6.8.1, and the distribution of tubes in the bottom dome is shown in Figure 6.8.2. The flow through the conduits proceeds from the furthest points from the detector into the skin. The flow in both the skin and TPC is upward, with the liquid collected in a set of equal-height weirs with a common drain. A central goal in all of these flows is to eliminate as far as practical any stagnant “dead” regions — the prime example of which would be the conduits if they were not purged. Such dead spaces, once impure, serve as a slow source of diffusively driven impurities that can greatly complicate purification. This is an issue not only for purity that affects charge and light collection, but also following the use of

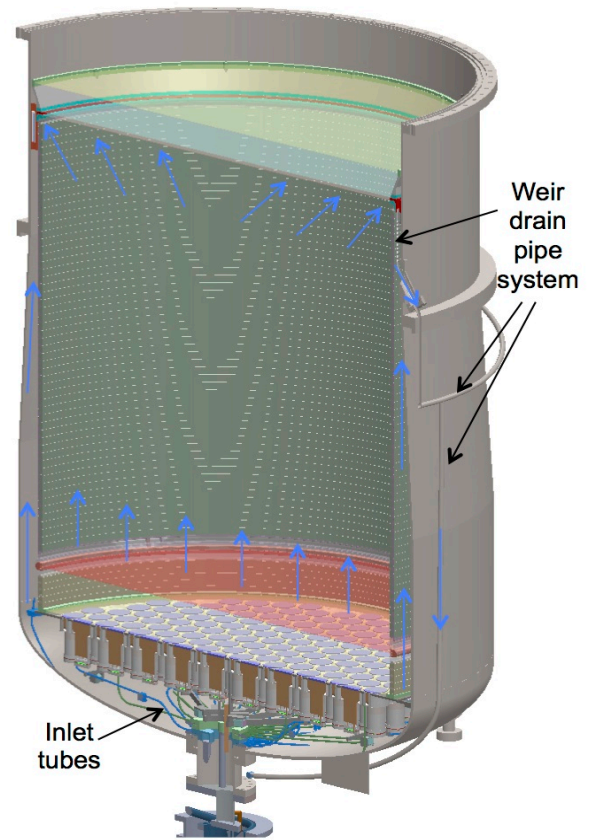


Figure 6.8.1. Schematic of the internal plumbing system, showing flows into the TPC and skin regions, and weir and drain system for LXe circulation in the TPC region, with flow direction sketched in blue.

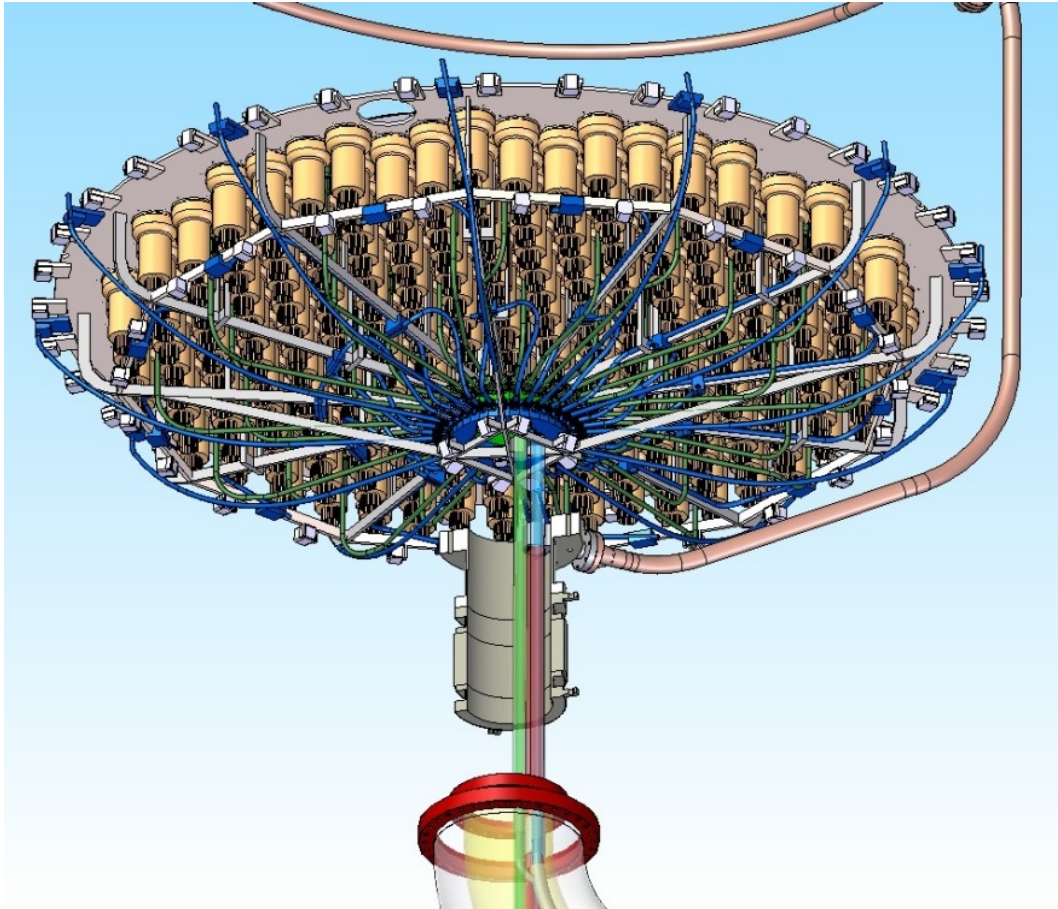


Figure 6.8.2. Fluid distribution in the bottom dome region. Fluid tubes in blue distribute flow into the dome and wall skin regions, while tubes in green distribute fluid into the TPC. The drain from the weirs is also shown — it transitions from inside the Xe vessel to the vacuum space and back into the Xe space below the dome, thus avoiding the highest field region of the skin.

radioactive tritium introduced as a calibration source (see Chapter 10), which must be subsequently removed.

We have chosen not to have any plumbing in the challenging high-field regions of the TPC. This limits locations where fluid lines can access the central TPC volume to the bottom PMT array, and to the perimeter of the TPC near the liquid surface, both of which regions have voltages near ground. We thus distribute the inlet tubes across the bottom PMT array holder, and line the circumference of the liquid surface with a set of weirs embedded into the wall of the TPC between the gate and anode grids. The placement of the inlet and outlets will be designed using computational fluid dynamics (CFD) to enable a uniform flow pattern. Similarly, the entry of fluid into the skin will be via a set of tubes that are distributed in the dome, with their placement again guided by CFD calculations.

These flows will also be used to control the operating temperature of the detector and, as much as possible, the thermal profile and behavior of the fluids throughout the system. The purification tower separately controls both the temperature and flow rate of the liquid in each flow path. The primary heat loads are on the wall of the vessel, the PMT bases, and the divider chains in the reverse and forward field sections of the TPC. The incoming fluid to the skin especially will provide the cooling to counter these heat loads and, guided by CFD.

An important goal is to obtain sufficient convective flow inside the detector to fully mix internal radioactive sources sufficiently quickly. An important source is $^{83\text{m}}\text{Kr}$, which we wish to have mixed on

the time scale of its 1.83 hour half life. Convection will likely be driven by some combination of the PMT base heaters attached to the bottom PMT array plate, and possibly by slightly warming the fluid returning to the TPC center. It is also possible that the flow of fluid can sufficiently drive convection. These issues will be studied in part using a full 3-D CFD simulation.

Initial cooling of the detector must be done with care in order to avoid large thermal gradients in the TPC structure, which has no obvious thermal anchor point. We thus plan to circulate Xe gas, cooled in the purification tower, to slowly cool the entire system at a controlled rate. We will make use of the separate flow streams in the TPC and skin, as well as the gas purge in the top dome area, and are using CFD to plan the rate of cooling. Sensors described in the next section will be used to monitor the cooling.

We also will attach two thermosyphon cooling (evaporator) heads directly to the inner vessel, one near the top and one near the bottom of the vessel. These will maintain detector temperature during any periods when we are not circulating fluid, but we do not anticipate them to be as effective in controlling the detector temperature as controlled fluid circulation.

The liquid level in the TPC and, secondarily, the skin is set by having both regions drain over a set of weirs. These weirs are integrated into a mechanical assembly that is integrated with the rings that hold the gate and anode grids, and which contains a common drain trough located at the top of the skin region: See Figure 6.2.1.6. A set of weirs drains Xe through slots in the plastic between gate and anode. The design of the weirs is simple, but their length must be selected carefully to avoid instability in flow over the lip, and to minimize the relationship between lip height and flow. This design will also be studied by CFD calculation, and will be tested in the system test (Section 6.10). The collection trough spans the circumference of the detector and is composed of three separate units, each of which has a separate drain line. These lines are routed outside the Xe vessel near the top of the liquid because we do not allow any mechanical elements, either conducting or nonconducting, in the skin in the vicinity of the HV cathode in order to maximize the HV standoff ability of the skin.

In addition to liquid circulation, we will have flows that purge all the spaces above the liquid: in the detector above the main surface both below and above the top PMT array; in the conduits above the dome; and above the bottom PMT conduit and HV conduit. The conduits must be purged because of the outgassing from the plastics in the cables in them, especially at their warm ends for which outgassing is orders of magnitude higher than from cold plastics. The gas above the detector will be circulated in a loop with controlled input and output flows, which we will operate in a balanced mode so that we neither evaporate nor condense liquid in the detector region. To ensure effective purge of the space above the liquid of the main TPC, this gas-purge system will use a set of tubes distributed in the top PMT array, in a manner similar to what is done on bottom array.

All tubing and associated fittings and weir structures in the skin of the vessel will be made from high-reflectivity PTFE so as to minimally interfere with light collection. All tubing and weir structures in the skin space will have as little optical footprint as possible.

6.9 Xenon System Monitoring

Several aspects of the detector require monitoring beyond that provided by PMT signals. Good resolution of the S2 signal relies on achieving a calm liquid surface at the right level, which we will monitor through precision level sensors, acoustic bubble sensors, and an optical inspection system. The thermal profile of the detector is an important aspect of liquid circulation and the stability of the liquid surface, and is measured by an array of thermometers. The ability of the system to sustain high voltages is very important and the optical system will help locate any sources of discharge, while a set of loop antennae will not only measure discharges but may also detect precursor signals to full discharge. Bubbles encountering a high-field surface can also lead to discharge, and so detection of bubbles is an important aspect of achieving high voltages. Finally, it is important to confirm that the significant thermal

contraction of the plastic field cage system behaves as expected, and so this motion will be monitored by a set of position sensors. This section discusses these monitoring systems in detail.

6.9.1 Thermometers

Temperatures need to be monitored at approximately 80 positions throughout the Xe detector and nearby. The chosen temperature sensor is a platinum (PT100-type) resistor, the precise make and shape of which is to be determined, taking into account installation and radioactivity level restrictions and constraints. The readout method is 4-wire throughout and the cabling to be used as much as possible is a semi-rigid polyimide-SS layered composite structure with parallel strip pairs inside and shielding/ground planes on the outside. The design of the semi-rigid cabling is individual to each sensor, or group of sensors. Semi-rigid cabling will be used inside the Xe and vacuum spaces to a maximum length of 1.5 meters, transitioning at connector blocks to conventional shielded 4-core wiring to cover the long stretches toward the breakout boxes, where mechanical robustness and threading capability is important. At the vacuum barriers of the breakout boxes, standard DB25 connectors are used, with 80 thermometers (320 wires) requiring at least 13 such connectors. The provision of DB25 connectors marks the interface to the slow-control work package (Chapter 11). Alternatively, higher-density connectors could reduce this number. More economic readout schemes, for example one in which some sensors are grouped and connected in series so that a common I+/I- wire pair can be used together with individual V+/V- taps on the thermometers, have been considered but dismissed as adding too much risk (a single wire failure could result in losing a whole group of thermometers). At positions where the potential effects of intrinsic component radioactivity are minimized, commercial pin headers and sockets can be used (black plastic is often a source of radioactivity). Nearer to the detectors, a combination of pins and clean PTFE, PEEK, or Delrin connector bodies should be used. The readout method implemented by the controls group will be based on modulating the sense current to avoid effects of thermo-power and other D.C. offsets. Calibration of the platinum resistors can be either via a generic table available for these, or individually tested together with the slow-control DAQ. Checks of intrinsic radioactivity levels are necessary, particularly for the PT100 and semi-rigid cabling near the main volume of the detector.

Cryogenic, laminated, layered semi-rigid cabling will likely be used for reading out at least the bulk of the thermometers. This cabling and the low-radioactivity connectors (if needed) can be made in-house with individual design for easy installation on site. The cable is based on polyimide/Kapton, to which stainless steel is laminated. These raw materials are etched to produce individual cabling and are laminated to receive shielding and ground layers on either side. A minimum track width of 150 μm and pitch of 300 μm can be achieved. The electronic capacitance between wire pairs is ~ 80 pF/m, depending on detailed geometry and operating temperature (via the temperature-dependent permittivity of Kapton).

6.9.2 Level Sensors

For level sensors, two main designs are needed: a parallel plate type for precision surface sensing, and long coaxial types. The precision surface sensor has the plates installed horizontally, straddling the boundary between the LXe and the electroluminescence region to measure the liquid level with high precision, allowing any tilt of the detector to be readily measured, and seeing variations in the liquid surface, for example from bubbles. Coaxial sensors monitor primarily the liquid levels during filling and emptying of the TPC and in the various elements of the purification tower. These sensors have been shown to work in principle, but detailed studies are still required to explore linearity, fringe field effects, systematics, capillary and meniscus effects, mechanical reproducibility, etc. The current design foresees three coaxial sensors that will span the height of the weir trough and the full 10-mm gate-anode distance, and three parallel plate sensors at the weir overflow openings. The sensors will be read out at high frequency with the aim of monitoring the condition of the Xe surface (level, ripples, waves) and, as such, will require a precision of ~ 10 μm . Further sensors will monitor the bottom skin region during filling and emptying, and a long level sensor will be used inside the PMT cabling standpipe to monitor the filling

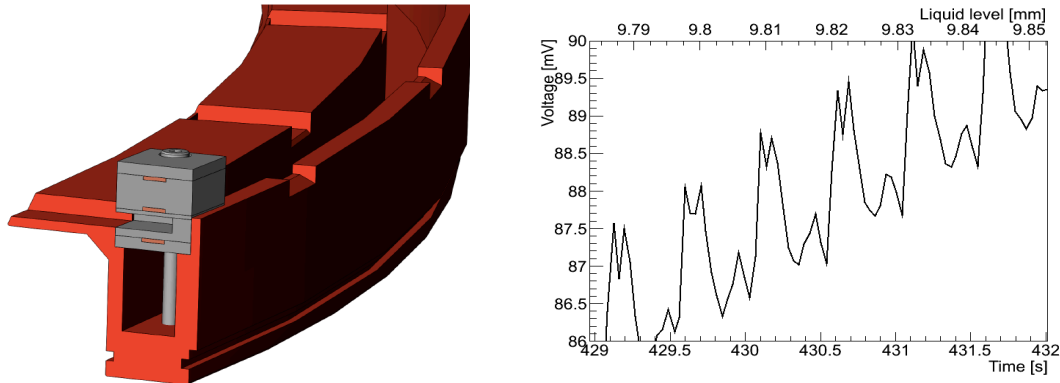


Figure 6.9.2.1. Left: Drawing of an example of a precision level sensor (gray with copper electrodes) situated in the weir region (red) of the LZ TPC. Any variation in the liquid level between the probe (middle) and excitation (lower) electrodes corresponds to a change in capacitance relative to the reference capacitance between the probe and inverse excitation (upper) electrode. Right: Response of a prototype sensor to an increasing liquid level created by accumulating drops of oil (with $\sim 8 \mu\text{m}$ level change per drop). Shown is an overall increase in the liquid level punctuated by excursions of measured voltage caused by the drops entering the container.

process. A pressure sensor at the bottom of the cryostat vessel will measure the head of the liquid and provide further information about the Xe level during filling and emptying. The readout method is via determination of capacitance with respect to a reference capacitance (all sensors employ three electrodes and a feedback readout circuit). This arrangement greatly reduces systematic effects arising from the long cabling in LZ and its variable capacitance (mechanical and thermal effects). The feedback readout circuit is the same as used for the position sensors and is based on modulated readout with a minimum number of analogue components and the bulk of front-end complexity absorbed into the firmware of a field-programmable gate array (FPGA). For feedthroughs at the vacuum barrier, a standard flange with sufficient numbers of coaxial connectors is foreseen. Each capacitive level or precision surface sensor requires three coaxial cables/feedthroughs. A drawing of a precision surface sensor and data from a prototype are shown in Figure 6.9.2.1.

6.9.3 Optical System

A system to carry out internal visual inspection at critical points is a powerful tool for monitoring the TPC. Small cameras exist and are most likely a cost-effective solution, but there is concern regarding radioactivity levels introduced by the presence of such cameras and their ability to operate at LXe temperatures. Both concerns require installation of cameras away from the TPC and at a higher temperature with optical systems (fibers, lenses, etc.) installed to transport the optical image from the internal region of the detector to the camera on the exterior of the cryostat. The cameras must be equipped to allow for temperature control as well as having an illumination system, to provide light inside the closed detector volume. This illumination can easily be supplied by LEDs. Ideally, such cameras are installed very close to or on the connector flange to the outside, with light guides and fibers installed internally. We plan to test this configuration on the system test stand (Section 6.10) before finalizing the design.

6.9.4 Acoustic Bubble Detection

A large range of acoustic sensors exists, based on different materials and physics effects. The best known are piezoelectric materials, but the majority of these are probably too radioactive to be acceptable. Another possibility is polymer film such as PVDT. Alternatively, sensors can be fabricated in-house from fully characterized materials. The sensors should be installed in contact with the outside of the Xe cryostat to pick up internal sound. The exact positioning of the sensors is to be determined through simulations of excitation modes of the vessel, supported by trials on existing systems, to determine the

optimum locations of the sensors. Eight sensors are foreseen, with three at 120° spacing near the lower cylindrical section of the cryostat, three near the top of that section, and one each on the top and bottom dome. The vacuum-barrier electrical connection is via a standard flange with a DB25 connector or individual coaxial connectors, to interface to dedicated readout electronics. Connection to slow control or faster DAQ is via optical fiber/USB standard solution. The readout will be continuous at 200 kS/s, or faster, to allow for sufficient bandwidth, properly anti-aliased at the analogue input, with further filtering and decimation in FPGA firmware. Also, triggers are necessary so that only data that are a clear departure from baseline noise are identified and transmitted downstream, i.e., allowing “significant events” to be recorded by slow control without necessarily recording the full data stream.

6.9.5 Loop Antennae for Discharge Detection

To monitor for the absence or occurrence of HV breakdown events, loop antennae capable of picking these up should be installed in critical positions. Care must be taken so that these metal aerials do not interfere with the presence of HV; therefore, eight such antennae will be installed on the top and bottom PMT trusses. A more detailed analysis on types and locations of possible HV breakdowns will further inform the exact positioning of these sensors. The antennae should be suitably decoupled via HV blocking capacitors or transformers before interfacing to fast-readout electronics. Cabling should be routed so as to not interfere with the HV present in the TPC. A standard flange with a set of coaxial or other high-speed signal feedthrough is required. The readout electronics will use fast sampling (200 MS/s), based on existing readout/optical fiber/USB interface system, with data reduction in an FPGA. Triggers for significant events will have to be developed.

6.9.6 TPC Alignment Sensors

Position sensors will be fitted on and around the top PMT array to monitor the thermal contraction and expansion of the TPC during cooling and warming, which is particularly large (~ 2 cm) in the vertical direction, as discussed in Section 6.2.3. Fitting capacitive parallel plate position sensors allows the

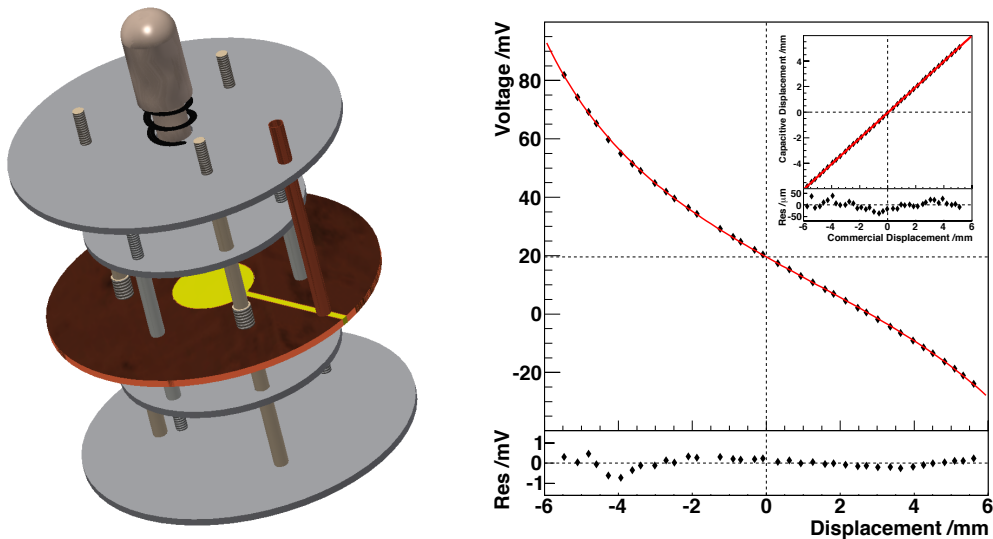


Figure 6.9.6.1. Left: Drawing of the position sensor. The top and bottom plates are guard plates and held at ground potential. Within these are the plates that carry the excitation signals. The central plate contains the sensing electrode (yellow) surrounded by a guard electrode that protects against the effects of fringe fields. The central plunger moves in and out, which varies the relative positions of the excitation electrodes to the sensing electrode. A central spring is used to allow a single fixed point. Right: (Main plot) Response of the sensor as a function of displacement fitted using the expected response function. The residuals of this fit are also shown. (Inset) The variables extracted from the fit to the response are used to calculate the displacement of the sensor vs. a commercial alternative, with residuals shown.

monitoring of vertical, horizontal, and helical motion of the TPC, giving vital information for determining whether and what countermeasures should be applied to ensure uniform cooling or warming of the TPC. These sensors are necessary because the alternative — equipping the length of the TPC with temperature sensors — is not feasible, as this would require readout wires to cross high-field regions. The position sensors are of simple design and are made from radiopure materials. The electronic readout is based on the same feedback circuit used in the level sensors, which acts to minimize the effect of cable capacitance on the sensor output. Eight sensors (three for vertical movement, three for horizontal movement, and two for helical movement) are planned. These sensors will also give important information on any lateral displacements that would alter the skin region gap, and the alignment of the top PMT array with respect to the TPC anchor points. The design of such a sensor and prototype test data are shown in Figure 6.9.6.1.

6.10 Integrated System Testing

A critical part of our planning is integrated or system testing of combined elements of key aspects of the Xe TPC and associated systems. The sections below summarize the smaller and then larger test systems available to the collaboration to evaluate critical aspects of the design of WBS 1.5 components and to test large-scale prototypes. Our testing plan is summarized in Section 6.10.6.

6.10.1 Study of Single Cathode Wires at High Field in Liquid Xenon

To ensure the successful delivery of HV to the LZ TPC, we take a comprehensive approach, beginning with an experimental study of the physics processes involved in the electric breakdown of individual cathode wires at a microscopic (quantum) level. A small double-phase Xe chamber was built and is now being operated at Imperial College London for this purpose. Instead of a cathode grid at the bottom of the liquid region, a single metal wire is used as a test sample. This configuration ensures that very high electric fields can be achieved at the wire surface by applying modest voltages of ~ 10 kV, approaching 300 kV/cm for a 100- μm sample, and ~ 1 MV/cm for 20- μm wire. The chamber has a single internal photomultiplier viewing down from the gas phase to detect both photon and charge emission from the upper surface of the wire sample. The electroluminescence response has single-electron sensitivity, allowing us to measure minute electron currents preceding macroscopic breakdown.

Most practical cathode electrodes in double-phase Xe detectors have been limited to surface fields of 40–65 kV/cm [17,28-32] — although the Xed chamber at Case Western Reserve University operated with substantially higher values of up to 220 kV/cm [33]. These fields are much lower than the published onset of electroluminescence or charge multiplication in the liquid, the former being 400–700 kV/cm for LXe [34,35]. The standard electrostatic design methodology adopted in previous experiments is therefore unsuitable and the adoption of a new “maximum allowable field” that can be sustained at the surface of metal surfaces must be conservative until new data can illuminate how to improve this. This justifies the currently adopted target value of 50 kV/cm.

Electron emission from metal surfaces can be caused by local enhancement of the electric field, the presence of thin insulating layers, or other effects that result in a lower effective work function. This can be accompanied by simultaneous photon emission. Our study focuses on the phenomenology associated with the onset of electrical breakdown. In particular, we are exploring its dependence on electric-field magnitude and direction, wire material, diameter, surface quality, history, etc. We will also investigate possible mitigation steps such as electropolishing, chemical etching, and conditioning in gas, to inform the production of the LZ wire grids.

This R&D activity employs the small chamber shown in Figure 6.10.1.1 (left) to test cathodes made from a single wire. The Xe vessel contains 4 kg of liquid in equilibrium with gas at 1.6 bar. Gate and anode grids 14 mm apart straddle the liquid surface, ensuring S2 yields that are mostly independent of the cathode voltage and sufficiently high for efficient cross-phase extraction and detection of single electrons. The 130-mm-long cathode wire is mounted 25 mm below the gate electrode, stretched between two

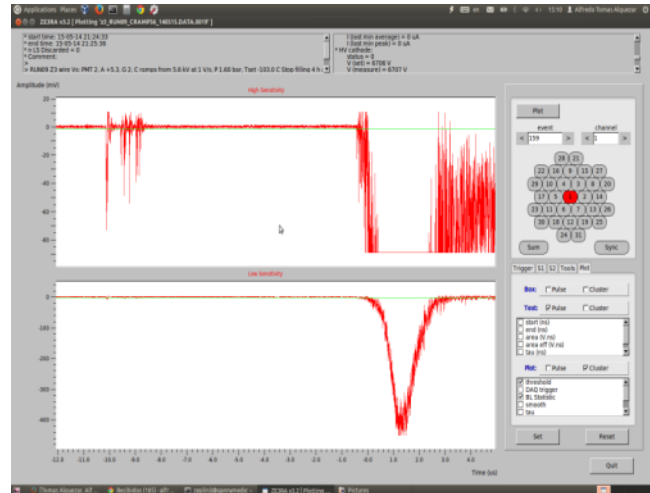
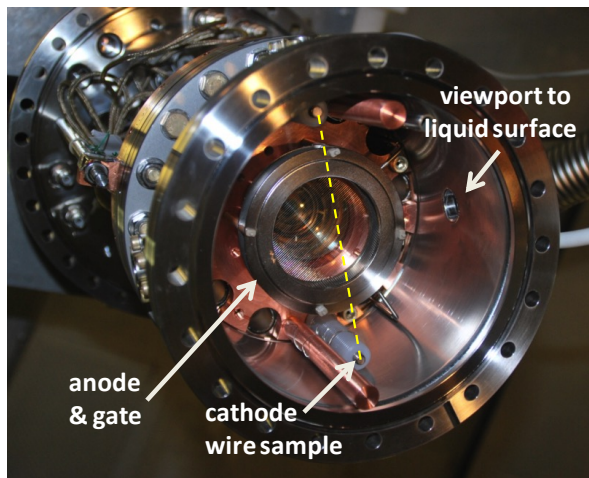


Figure 6.10.1.1. Left: Internal view of Imperial LXe chamber looking up from below. A photomultiplier is just visible through the gate and anode grids, which establish electroluminescence above the liquid surface (nominally located between them). The cathode wire sample (highlighted) is stretched between the two feedthroughs shown. Right: A typical waveform, probably unrelated to discharge, recorded with a sample of 100 μm ZEPLIN-III wire with ~ 145 kV/cm on the wire surface. A large S2-like signal (seen clearly in the lower, low-sensitivity channel) is preceded by an S1-like optical pulse and a single electron cluster.

feedthroughs that can deliver up to -10 kV to the liquid. The electric field is highest on the upper surface of the sample, so that any electron emission is likely to lead to electroluminescence signals in the gas.

Most subsystems required to operate the chamber were inherited from the ZEPLIN-III experiment (gas handling and purification, slow controls, data acquisition). The ZE3RA data-reduction software allows full exploitation of the 2-ns-sampled waveforms [36], which are recorded in high- and low-sensitivity channels to cover both very small signals and larger S1 and S2 pulses.

The chamber is cooled by means of a 1-inch cold finger immersed in liquid nitrogen, providing 10–15 W of cooling power and autonomy of 7–9 hrs between LN fills, and very simple and reliable operation. Prior to condensing, the Xe gas is purified with a heated SAES getter for approximately one week to ensure sufficient electron lifetime (≥ 20 μs) during the test. Cooldown is achieved overnight, and the chamber is filled, operated, and emptied in a single day.

Prior to the cathode test, the gate-anode system is biased to establish two-phase operation. Then the voltage applied to the wire sample is ramped up slowly (~ 1 V/s) to several kV until the power supply trips, with PMT data being digitized simultaneously. This voltage and other slow-control data are embedded with the main data set for analysis. Electron emission from the cathode can, if accompanied by prompt light, be reconstructed to the cathode depth by electron drift time. A sample of the 100- μm wire used in ZEPLIN-III has already been tested and observed to reach 145 kV/cm before tripping. Figure 6.10.1.1 (right) shows an event acquired close to the trip voltage, showcasing the types of pulses we can measure: from left to right, an S1-like pulse from prompt light, then a small cluster of photoelectrons corresponding to a single emitted electron, and finally a large S2 pulse delayed by ≈ 10 μs . Most other events close to breakdown feature more complicated topologies that we are now analyzing. This breakdown field is clearly much higher than achieved in ZEPLIN-III with the same type of wire — which sustained stably 62 and 40 kV/cm in the first and second runs, respectively [29,31]. However, we point out that the total length of the ZEPLIN-III cathode wire was 117 meters, which is probably a very relevant parameter.

We will continue to test wires before and after treatment, in particular to try to understand the origin of photon and electron emission around the early onset of instability. We plan to examine wire samples from Xed [33], LUX gate and cathode grids [17], and candidate wires for LZ. Apart from SS, we will consider

beryllium copper and tungsten, as well as coated samples (gold, silicon nitride, etc.). Small- and medium-scale wire grids can then be built and tested as described below.

6.10.2 Study of Bare Cathode Frames and Gridded Cathodes at High Field in Liquid Xenon

In concert with the efforts described in Section 6.10.1, we plan additional studies of the onset and origin of photon emission in high electric fields in LXe. These studies will utilize small dual-phase LXe emission detectors at institutions within the LZ collaboration. An example at LBNL is shown in Figure 6.10.2.1. This test bed is functionally similar to that described in Section 6.10.1, but with the ability to evaluate small cathode wire planes consisting of an SS frame and stretched wires.

Initial tests will study the maximum surface electric field that can be applied to the cathode frame alone, in the absence of wires. This is clearly an important test, as the cathode frame is a requisite component in deploying a gridded TPC. Subsequent tests will study the maximum surface electric field with a single grid wire stretched across the diameter of the frame. As long as effects from the frame are subdominant, these studies should obtain results that can be cross-checked with those from Section 6.10.1. Separate samples of wire have been obtained for these studies, with a focus on SS, beryllium copper, and gold-coated tungsten. The effect of surface treatments such as electropolishing will also be explored.

Given the importance of a robust expectation for electric-field performance in LZ, we intend full duplication of the study of all wire samples and surface preparations. We also will search for effects due to LXe liquid purity, temperature, and thermodynamic history.

A final step in this program will be to string complete small cathodes and verify their performance in terms of the maximum surface electric field that can be sustained prior to the onset of photon emission. A key question is whether this performance can be simply inferred from the single-wire studies, or if (as stated in Section 6.10.1) the length of wire is in fact a critical parameter. A complete cathode grid frame will allow an approximate factor-of-10 increase in wire length compared with a single wire. A dependence on wire length would point clearly to the importance of a more aggressive surface finish and treatment program, with continued testing as already described. A series of other tests using small test chambers available to the collaboration are also planned over the next year. These will include component, PMT base and temperature, and other sensor testing in LXe.

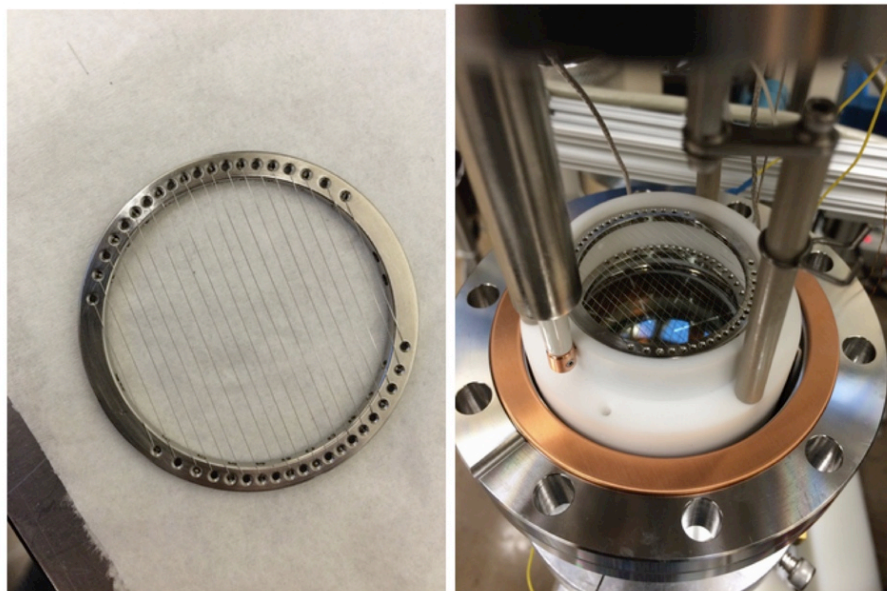


Figure 6.10.2.1. Left: Example of a wire grid that will be tested in the small LBNL test chamber or other test chambers. Right: View of the LBNL test chamber.

6.10.3 Large-scale High-voltage Testing of Critical Assemblies in Liquid Argon

Three assemblies in the LZ detector must accommodate the large negative-cathode voltage. These are the forward-grading structure (connecting the cathode grid to the gate grid), the reverse-grading structure (connecting the cathode grid to the bottom grid), and the cable-grading structure (connecting the cathode grid to the grounded shield of the cathode HV cable). Each structure contains a series of conductive rings connected by resistors to produce a controlled grading of the voltage. It is critical that these assemblies sustain the applied cathode voltage without producing light from electrical discharges across their components or to the inner wall of the cryostat. We have developed a large-scale system for testing these critical assemblies at HV in liquid argon, which acts as a cost-effective proxy for LXe. A schematic view of the setup is shown in Figure 6.10.3.1 (left) and dewar and HV connection (right).

The HV tests are performed within a 240-liter cryogenic dewar of 16-inch bore. The assembly under test is supported from below by a platform that hangs from the top flange of the dewar. The bottom of the tested assembly is grounded by the platform; the top is connected to HV that can be ramped to -200 kV to simulate the LZ cathode. The HV is delivered through a polyethylene cable that originates at a feedthrough located 8 feet above the top of the dewar. The feedthrough is connected to a DC power supply made by Glassman High Voltage. A controlled electrostatic environment is maintained around the test assembly by surrounding it with a highly transparent grounded metal mesh that shields any nearby structures. Seven lenses at various angles view the assembly from just outside the mesh. These are connected to fiber bundles that route the images to a charge-coupled device (CCD) camera located just above the top flange of the dewar, providing a real-time view of any electrical discharges that occur during testing. Below the tested assembly is a quartz window coated with fluorescent tetraphenyl

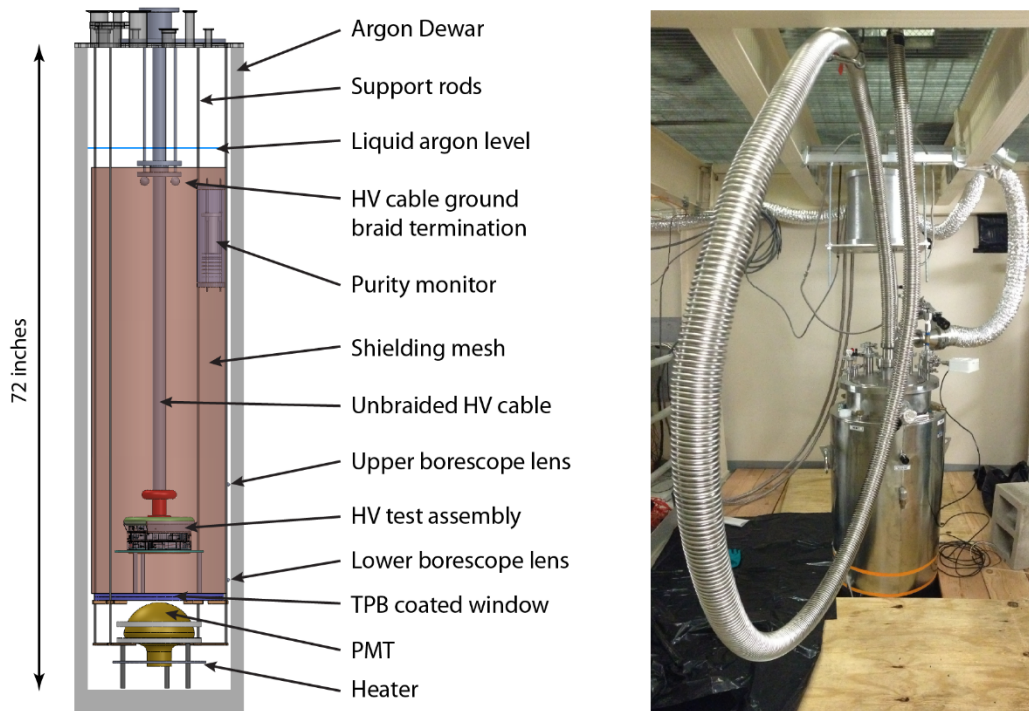


Figure 6.10.3.1. Left: Side view showing the internal components of the liquid argon test system. Note that the vertical support rods (shown out-of-plane in this view) are positioned outside the shielding mesh. For clarity, only two of the seven borescope lenses are shown. The HV test assembly shown here is a portion of the grading structure of the reverse-field region of the detector. Right: The liquid argon dewar and HV cable conduit at Yale University. The HV feedthrough sits above the square hole in the steel grating at the top of the image.

butadiene (TPB) wavelength shifter. This window is viewed by an 8-inch-diameter PMT, giving efficient detection of ultraviolet light with single-photon sensitivity.

Commercially available liquid argon typically contains impurities of 10 ppm. These are known to substantially enhance the dielectric strength of liquid argon, and must be removed before making meaningful tests [37]. The dewar is filled with commercially available liquid argon that is passed through a liquid phase purification system based on molecular sieve and activated copper filters [38]. The purity of the argon is measured at the top of the dewar by a compact monitor based on a device developed by the ICARUS collaboration [39]. Conversion electrons from a ^{207}Bi source ionize liquid argon in an applied electric field. The resulting electrons are drifted through two charge-sensing regions separated by a 6-cm distance. A charge-sensitive amplifier measures the charge induced by the electrons in the two regions to infer the fraction of electrons lost while drifting between them. The electron lifetime is then computed from the lost fraction and the time required to traverse the 6-cm distance. The monitor is sensitive to lifetimes less than 100 μs , corresponding to 2.5 ppb of oxygen.

In a typical testing cycle, the tested HV assembly is mounted to the platform that hangs below the top flange of the dewar. The top flange is then lowered by crane into the argon dewar. The HV cable is then lowered through a port on the top flange until it engages a socket at the top of the test structure. The dewar is flushed with argon gas, evacuated, and filled over several hours with purified liquid argon. High voltage can be applied once the liquid argon has submerged the termination of the HV cable braid, with ramping to full voltage requiring a few hours. A 1-kW heater is used to boil the argon at the bottom of the dewar after HV testing. The HV cable and top flange are removed once the dewar is warm. This arrangement allows for testing of a unique assembly every four days, allowing for rapid design iteration of the critical HV assemblies.

6.10.4 Case Western and SLAC Test Systems

The large-scale components whose test in liquid argon is discussed in the previous section must ultimately be tested in LXe. A challenge for such tests is the cost of and complexity of handling large amounts of LXe systems. Test systems must therefore accommodate TPC test structures that are as narrow as possible while still maintaining the high electric fields in the critical region around the cathode that will be encountered in LZ, and also allow a full test of the reverse-field region. Construction of the LXe test system is planned in two phases.

In Phase I, a 10-inch-diameter vessel is used to test a version of TPC structure discussed in Section 6.10.6 with an overall height up to 70 cm, and requiring roughly 100 kg of LXe. We anticipate operating this system at voltages up to 100 kV. The Phase I testing platform, shown in Figure 6.10.4.1, has been developed at Case Western, and is being commissioned at SLAC, where the Case group has relocated. The system has two basic architectural features in common with LZ: a separate purification tower housing a heat-exchanger system connected to the main vessel via a vacuum-insulated plumbing run below both vessel sets; and a side-entry HV feedthrough at the cathode level. The HV feedthrough system uses a commercial 100-kV ceramic feedthrough installed on a side port directly on the cold vessel. One part is immersed in LXe, while the nominal vacuum side is on the exterior and immersed in Fluorinert FC-770. This is an insulating fluorocarbon with good dielectric properties, and is liquid at both room temperature and at 165 K. A commercial >100-kV-rated HV cable is immersed in this fluid for the run between cryogenic and room temperatures, and continues uninterrupted to a commercial power supply.

The implementation of the TPC prototype in this vessel is driven by many of the same constraints as LZ, and shares several features. It has an HV standoff skin layer of LXe whose thickness is the minimum needed to achieve sufficiently low electric fields on all HV surfaces. Cabling and plumbing feedthroughs are located on both the top and bottom of the vessel (visible in Figure 6.10.4.1) so that the skin has no cables or fluid lines in the HV region around the cathode. In addition, the fluid circulation will use a weir system based on the LZ design. The test platform has ample breakout hardware for multiple PMTs, level sensors, thermometers, and other instrumentation such as loop antenna discharge sensors. We plan to

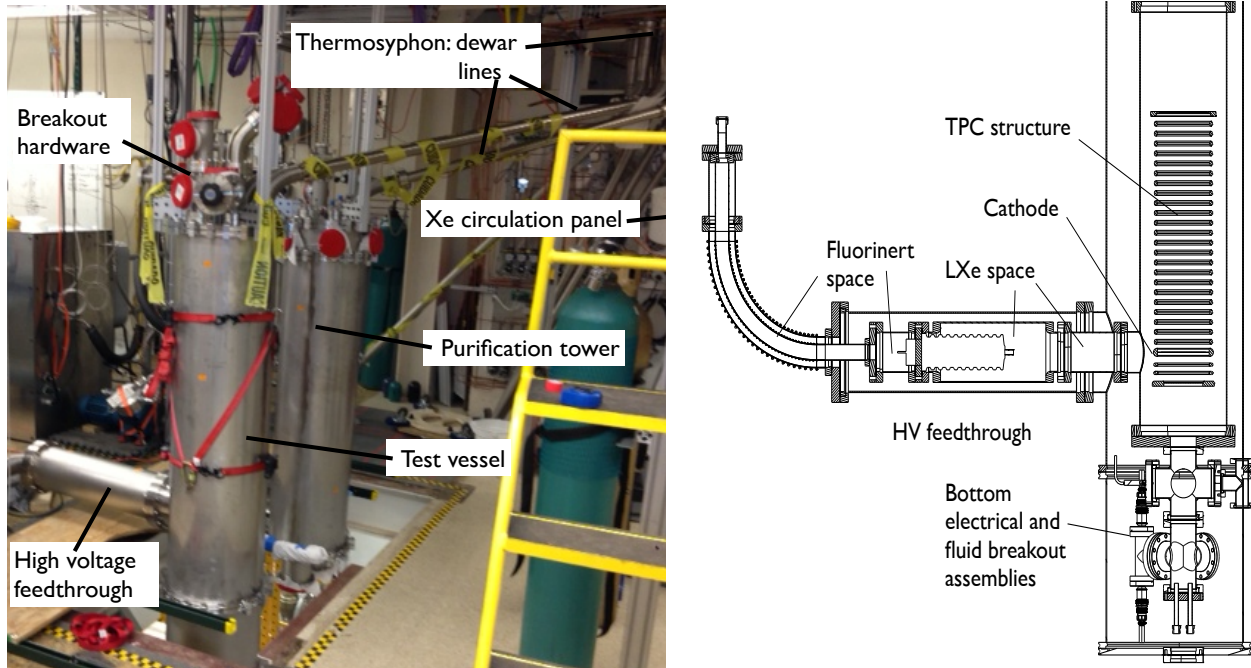


Figure 6.10.4.1. Left: Phase I system. Right: Cross-section view of the Phase I test vessel showing the HV feedthrough and TPC structure installed.

outfit the TPC with a PMT at the top and bottom with conical reflectors. This will allow a two-phase S1/S2 readout that will provide a highly sensitive measure of Xe purity. We will also deploy a version of the camera system being developed at Texas A&M (Section 6.10.5) and also being deployed in the Yale system to image discharge phenomena.

In Phase II, a significantly larger vessel with a nominal 18-inch diameter that requires some 500 kg of LXe will be used to test a larger TPC structure. The cathode of this TPC can be operated at the full 200-kV design voltage of LZ. Once again, the radius of the vessels and the thickness of the Xe skin are sufficient to reproduce the final fields that LZ will have in the cathode region, and to test the reverse-field region at full voltage. Critically, the cryostat will be sized to accommodate a copy of the full-size LZ HV feedthrough system.

The staging of both phases at SLAC is shown in Figure 6.10.4.2. The former BaBar counting room and surrounding space in the IR2 experimental hall is being renovated for the purpose of hosting this system, providing ample room for operations and later expansion. The vessels will be deployed under HEPA units so we can establish a soft-wall clean area. The support systems for these test vessels, partially visible in Figure 6.10.4.1 (left) and Figure 6.10.4.2, are extensive. They build on developments from LUX and ZEPLIN and serve as prototypes of what will be used on LZ. Cryogenics for both phases are supplied by a



Figure 6.10.4.2. The System Test Platform housed at the former counting room for BaBar at SLAC.

thermosyphon “backbone,” which consists of a multiport thermosyphon dewar capable of providing more than 12 separate PID (proportional-integral-derivative controller)-controlled cooling heads. Two will be used for each vessel set, and one or more in the purification tower, with several more used for automated cold traps in the gas-handling and -sampling systems. The purification tower will include prototypes of the elements of the circulation system planned for LZ: a weir reservoir, two-phase heat exchanger, gas-phase heat exchanger, and a “subcooling” thermosyphon head on the condensing stream, along with an extensive set of fluid level sensors and thermometers.

The system for online purification through a hot getter uses highly automated gas-handling panels based on ½-inch-diameter tubing that will accommodate flow rates well in excess of 100 slpm. This will (1) allow the large test platforms to achieve higher purity quickly (by contrast, LUX, with 300 kg, circulates Xe at roughly 25 slpm), allowing faster testing cycles; and (2) allow tests of the heat-exchange system at high flow rates. This system also features a high-flow capacity metal diaphragm compressor as the circulation pump. This technology allows very high flow rates and has been identified (WBS 1.4 and Chapter 9) as the technology for LZ, but to our knowledge has not been used in any previous similar Xe experiment. Thus, the system will provide an important test of these pumps.

Critical elements of control and fail-safe recovery of the Xe will also be developed as part of the system test platform, including integration of process loop controllers (PLCs) for critical systems and integration with larger slow-control system development. Phase I Xe recovery uses a thermosyphon-driven storage and recovery vessel patterned on a similar device used for LUX. For Phase II, we will use a compressor-based recovery into standard storage cylinders, as is planned for LZ. This requires a highly reliable system with generator-based backup power. For Phase II, we will also deploy a passive recovery “balloon” for final fail-safe recovery and containment of the 500 kg of Xe. Elements of the planned LZ online and slow-control systems will be developed for the system test to allow a high degree of test automation. The gas system is also designed to be closely integrated with an automated, high-sensitivity purity-monitoring system initially developed by the Maryland group. This will be important in order to achieve purity for successful HV testing; it will also allow us to check our understanding of various factors that will be important for LZ purification. Finally, the system is designed to accommodate the range of gaseous radioactive calibration sources deployed in LUX and planned for LZ.

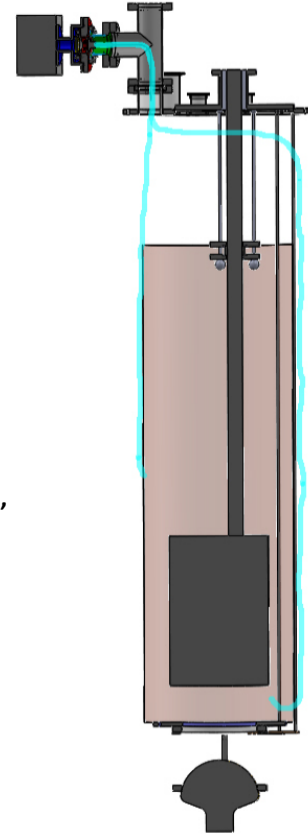
6.10.5 Camera Systems

The camera system discussed in Section 6.9.3 is first being deployed as an essential part of the System Test, and so is further described here. Two-phase Xe operation requires a series of grids and field-shaping rings at different voltages that provide a uniform drift region and electron extraction from a nonturbulent LXe surface. While the design goes to great lengths to minimize problems, sparking or turbulence (perhaps bubbling) could occur, and it is important to understand the cause and location. While some problems can be detected by the photomultipliers and capacitive level sensors, visual inspection of the location of possible sparks and observation of bubbles or floating contaminants has clear advantages. The Texas A&M group has designed, built, and tested at LN temperatures a prototype system that includes a CCD camera to record images from a coherent fiber-optic bundle, which can view the entire active region of the system test TPC (see Figure 6.10.5.1). The plan for the system test is to build a multifiber bundle to attach to this camera to enable inspection of up to seven regions inside the cryostat. This multibundle fiberscope will allow inspection of the TPC internal region, HV feedthrough region, reverse and forward field regions during the commissioning, and operation of the system test stands.

A sketch of the proposed system is shown on the right in Figure 6.10.5.1, indicating the location of the CCD camera and the fiber bundles that will be used to observe the space inside the liquid argon system test cryostat. A similar camera and fiber configuration is being planned for the SLAC System tests using LXe. Both systems will have seven 0.72-mm silica fiber bundles containing 30,000 fibers to view the internals of the detector. These fibers will be arrayed in a 2-3-2 close-packed arrangement and imaged on the CCD plane of the camera.



Figure 6.10.5.1. Above: Disassembled camera setup. From left, they are: camera, F-C mount converter, telecentric lens, camera/optical fiber adapter (disassembled). Beneath: Optical fiber.



Right: Survey camera arrangement proposed for the Yale system test stand. The camera is at the top left of the figure and the blue lines indicate the locations of the fibers inside the cryostat.

6.10.6 Summary of Integrated Testing Plans

The testing capabilities and facilities described above will be used to test critical prototype elements of the TPC and HV systems. The first goal of these integrated tests is to demonstrate that the TPC field cage structure and grids can reach the electric fields required. Below is a brief description of these phased tests. Prototype TPC structures are under construction, to be tested both in liquid argon at Yale and in LXe at SLAC. Models of these prototypes are shown in Figure 6.10.6.1. The model shown on the left is a

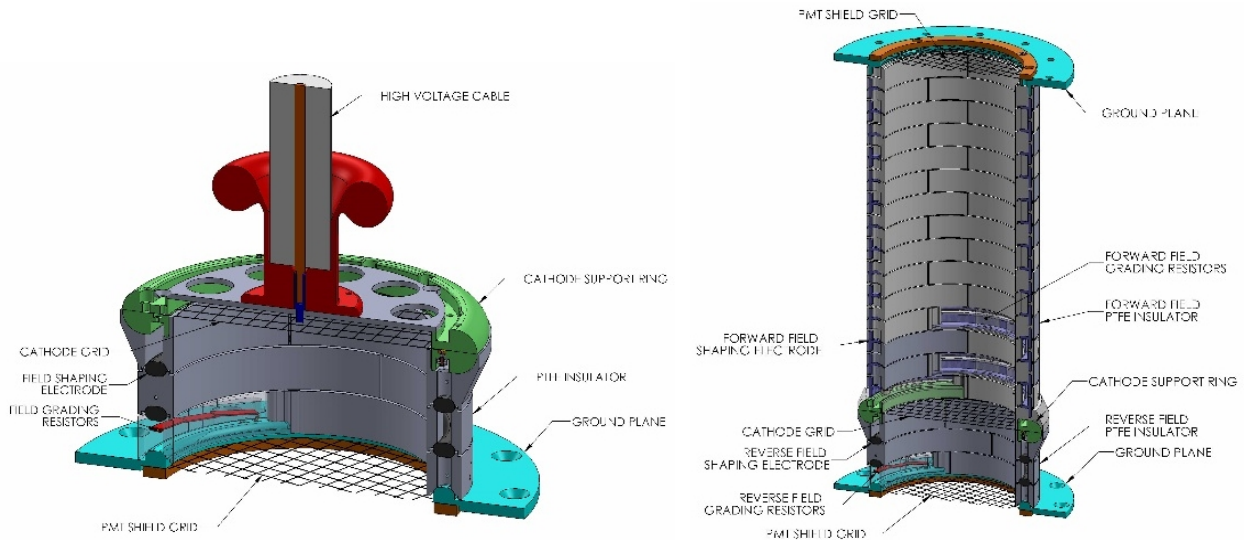


Figure 6.10.6.1. Left: Phase I, reverse-field region prototype described in the text. Right: Schematic of larger-scale TPC and HV grid prototypes that would be tested in a phased approach described in the text.

prototype of the reverse-field region of the TPC as it would be tested initially (Section 6.10.3) and uses the camera system described in Section 6.10.5. A prototype of the HV cable would first be connected to a simple plate at the top of the structure and operated up to 100 kV. This prototype is designed so that 100 kV simulates the electric fields seen in LZ at 200 kV and thus would test the TPC design under these conditions. A second version of this prototype would subsequently and possibly concurrently be operated in the Phase I LXe test system at SLAC (Section 6.10.4), albeit in a different HV configuration and taking into account lessons from the tests in liquid argon. Parts for two of these TPC prototypes have been fabricated primarily by LBNL. Prototype grid structures may also be tested in this prototype and these would be informed by the single-wire and small-grid testing described previously.

Ultimately, a larger-scale TPC prototype would be tested in the Phase II LXe test system at SLAC and possibly a version tested in liquid argon at Yale, depending on what is measured in Phase I prototype testing. This Phase II prototype is shown in Figure 6.10.6.1 (right) and would incorporate realistic grid structures, updated designs for the TPC structure, and other features. Prototype internal temperature, level, and other sensors would be included. The primary purpose of this prototype program would be to verify most aspects of HV operation in a realistic structure. However, operation in S2/S1 mode with purification and PMT readout would be the long-term goal and thus this would become a test bed for additional studies during the fabrication of the LZ components.

Chapter 6 References

- [1] D. S. Leonard *et al.*, *Nucl. Instrum. Meth.* **A591**, 490 (2008), arXiv:0709.4524 [physics.ins-det].
- [2] (2014), EXO collaboration, private communication.
- [3] W. Blum, W. Riegler, and L. Rolandi, *Particle Detection with Drift Chambers*, Particle Acceleration and Detection (Springer Berlin Heidelberg, 2008).
- [4] K. McDonald, “Notes on electrostatic wire grids,” (2003), (unpublished).
- [5] Y. Mei, *Direct Dark Matter Search with the XENON100 Experiment*, Ph.D. thesis, Rice University (2011).
- [6] D. Akerib, H. Araújo, E. Bernard, C. Ghag, D. McKinsey, C. Sofka, S. Pereverzev, J. Va’vra, W. Waldron, and J. White, *High Voltage Task Force Report*, Tech. Rep. (LZ Collaboration, 2013).
- [7] U.S. Department of Energy, *DOE Handbook: Electrical Safety*, Tech. Rep. DOE-HDBK-1092-2013 (Forrestal Building, 1000 Independence Avenue, SW, Washington, DC 20585-0002, USA, 2013).
- [8] D. S. Akerib *et al.* (LUX), *Nucl. Instrum. Meth.* **A703**, 1 (2013), arXiv:1205.2272 [physics.ins-det].
- [9] K. Nakamura, Y. Hamana, Y. Ishigami, and T. Matsui, in *1st International Conference on Technology and Instrumentation in Particle Physics, TIPP09, Tsukuba, Japan, March 12-17, 2009*, *Nucl. Instrum. Meth.*, Vol. **A623** (2010) pp. 276–278, *Latest bialkali photocathode with ultra high sensitivity*.
- [10] D. C. Malling, *Measurement and Analysis of WIMP Detection Backgrounds, and Characterization and Performance of the Large Underground Xenon Dark Matter Search Experiment*, Ph.D. thesis, Brown University (2014).
- [11] E. Aprile *et al.* (XENON1T), “Lowering the radioactivity of the photomultiplier tubes for the XENON1T dark matter experiment,” (2015), arXiv:1503.07698 [astro-ph].
- [12] E. Aprile *et al.* (XENON10), *Astropart. Phys.* **34**, 679 (2011), arXiv:1001.2834 [astro-ph].
- [13] V. N. Solovov *et al.* (ZEPLIN-III), in *Nuclear Science Symposium and Medical Imaging Conference (NSS/MIC), 2011 IEEE* (2011) pp. 1226–1233, *Position Reconstruction in a Dual Phase Xenon Scintillation Detector*; V. N. Solovov *et al.* (ZEPLIN-III), *IEEE Trans. Nucl. Sci.* **59**, 3286 (2012), arXiv:1112.1481 [physics.ins-det].
- [14] D. W. Lynch and W. Hunter, in *Handbook of Optical Constants of Solids*, edited by E. D. Palik (Academic Press, Burlington, 1997) pp. 233–286.
- [15] R. French *et al.*, *Solar Energy Materials and Solar Cells* **95**, 2077 (2011).
- [16] E. Santos *et al.* (ZEPLIN-III), *J. High Energy Phys.* **2011**, 115 (2011), arXiv:1110.3056 [physics.ins-det].
- [17] D. S. Akerib *et al.* (LUX), *Phys. Rev. Lett.* **112**, 091303 (2014), arXiv:1310.8214 [astro-ph].
- [18] A. Fonseca, R. Meleiro, V. Chepel, A. Pereira, V. Solovov, and M. Lopes, in *Nuclear Science Symposium Conference Record, 2004 IEEE*, Vol. **1** (2004) pp. 572–576, *Study of secondary scintillation in xenon vapour*.
- [19] E. Gushchin, A. Kruglov, V. Litskevich, A. Lebedev, and I. Obodovski, *Sov. Phys. JETP* **49**, 856 (1979), [*Zh. Eksp. Teor. Fiz.* **76**, 1685 (1979)].
- [20] F. P. Santos, T. H. V. T. Dias, A. D. Stauffer, and C. A. N. Conde, *J. Phys. D: Appl Phys.* **27**, 42 (1994).
- [21] S. F. Biagi, *Nucl. Instrum. Meth.* **A421**, 234 (1999), (Magboltz).
- [22] R. Veenhof, in *Programming and mathematical techniques in physics. Proceedings, International Conference on programming and mathematical methods for solving physical problems, June 14-19, 1993, Dubna, Russia*, Conf. Proc., Vol. **C9306149** (1993) pp. 66–71, (Garfield++).
- [23] M. Lyly, J. Ruokolainen, and E. Järvinen, *ELMER - A finite element solver for multiphysics*, Tech. Rep. (CSC - IT Center for Science Ltd., P. O. Box 405, FI-02101 Espoo, Finland, 1999-2000) (Elmer).
- [24] C. Geuzaine and J.-F. Remacle, *Int. J. Numer. Meth. Eng.* **79**, 1309 (2009), (Gmsh).

- [25] E. Aprile *et al.* (XENON100), *Astropart. Phys.* **35**, 573 (2012), arXiv:1107.2155 [astro-ph].
- [26] D. Yu. Akimov *et al.* (ZEPLIN-III), *Astropart. Phys.* **27**, 46 (2007), arXiv:astro-ph/0605500 [astro-ph].
- [27] J. B. Albert *et al.* (EXO-200), *Nature* **510**, 229 (2014), arXiv:1402.6956 [nucl-ex].
- [28] A. S. Howard (UK Dark Matter), in *Nonaccelerator new physics. Proceedings, 4th International Conference, NANP '03, Dubna, Russia, June 23-28, 2003*, *Phys. Atom. Nucl.*, Vol. **67** (2004) pp. 2032–2040, *Dark matter searches by the Boulby Collaboration and liquid xenon prototype development*.
- [29] V. N. Lebedenko *et al.* (ZEPLIN-III), *Phys. Rev.* **D80**, 052010 (2009), arXiv:0812.1150 [astro-ph].
- [30] A. A. Burenkov, D. Yu. Akimov, Yu. L. Grishkin, A. G. Kovalenko, V. N. Lebedenko, V. N. Solovov, V. N. Stekhanov, F. Neves, and T. J. Sumner, *Phys. Atom. Nucl.* **72**, 653 (2009), [*Yad. Fiz.* 72,693(2009)].
- [31] D. Yu. Akimov *et al.* (ZEPLIN-III), *Phys. Lett.* **B709**, 14 (2012), arXiv:1110.4769 [astro-ph].
- [32] D. Yu. Akimov *et al.*, *Instrum. Exp. Tech.* **55**, 423 (2012), [*Prib. Tekh. Eksp.* 2012,no.4,6(2012)].
- [33] T. Shutt, A. Bolozdynya, P. Brusov, C. E. Dahl, and J. Kwong, in *Dark Matter 2006. Proceedings of the 7th UCLA Symposium on Sources and Detection of Dark Matter and Dark Energy in the Universe*, *Nucl. Phys. Proc. Suppl.*, Vol. **173** (2007) pp. 160–163, *Performance and Fundamental Processes at Low Energy in a Two-Phase Liquid Xenon Dark Matter Detector*, arXiv:astro-ph/0608137 [astro-ph].
- [34] S. E. Derenzo, T. S. Mast, H. Zaklad, and R. A. Muller, *Phys. Rev.* **A9**, 2582 (1974).
- [35] K. Masuda, S. Takasu, T. Doke, T. Takahashi, A. Nakamoto, S. Kubota, and E. Shibamura, *Nucl. Instrum. Meth* **160**, 247 (1979).
- [36] F. Neves *et al.* (ZEPLIN-III), *J. Instrum.* **6**, P11004 (2011), arXiv:1106.0808 [astro-ph].
- [37] E. Bernard, C. H. Faham, T. M. Ito, B. Lundberg, M. Messina, F. Monrabal, S. P. Pereverzev, F. Resnati, P. C. Rowson, M. Soderberg, T. Strauss, A. Tomas, J. Va'vra, and H. Wang, in *High Voltage in Noble Liquids for High Energy Physics*, *J. Instrum.*, Vol. **9**, edited by B. Rebel and C. Hall (2014) p. T08004, arXiv:1403.3613 [physics.ins-det].
- [38] A. Curioni, B. T. Fleming, W. Jaskierny, C. Kendziora, J. Krider, S. Pordes, M. P. Soderberg, J. Spitz, T. Tope, and T. Wongjirad, *Nucl. Instrum. Meth.* **A605**, 306 (2009), arXiv:0903.2066 [physics.ins-det].
- [39] S. Amerio *et al.* (ICARUS), *Nucl. Instrum. Meth.* **A527**, 329 (2004).